Non-Faradaic Energy Storage by Room Temperature Ionic Liquids in Nanoporous Electrodes

Jenel Vatamanu,* Mihaela Vatamanu, and Dmitry Bedrov*

Material Sciences and Engineering Department, University of Utah, 122 South Central Campus Drive, Salt Lake City, Utah 84112, United States

ABSTRACT The enhancement of non-Faradaic charge and energy density stored by ionic electrolytes in nanostructured electrodes is an intriguing issue of great practical importance for energy storage in electric double layer capacitors. On the basis of extensive molecular dynamics simulations of various carbon-based nanoporous electrodes and room temperature ionic liquid (RTIL) electrolytes, we identify atomistic mechanisms and correlations between electrode/electrolyte structures that lead to capacitance enhancement. In the symmetric electrode setup with nanopores having atomically smooth walls, most RTILs showed up to 50% capacitance increase compared to infinitely wide pore. Extensive simulations using asymmetric electrodes and pores with atomically rough surfaces demonstrated that tuning of electrode nanostructure could lead to further substantial capacitance enhancement. Therefore, the capacitance in nanoporous electrodes can be increased due to a combination of two effects: (i) the screening of ionic interactions by nanopore walls upon electrolyte nanoconfinement, and (ii) the optimization of nanopore structure (volume, surface roughness) to take into account the asymmetry between cation and anion chemical structures.

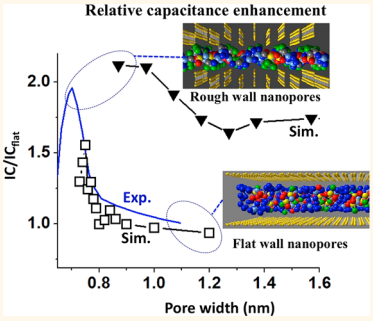

KEYWORDS: energy storage · supercapacitors · room temperature ionic liquids · nanoporous electrodes · capacitance · electric double layer · nanoconfinement

The electric double layer capacitors (EDLCs), or supercapacitors, made of porous carbon-based electrodes and room temperature ionic liquid (RTIL) electrolytes, have attracted considerable attention as promising energy storage devices. The combination of advantages provided by RTIL electrolytes (*e.g.*, low volatility[1,2] and flammability,[3] good ionic conductivity,[4,5] good chemical and electrochemical stability[6−11] and high thermal stability[12−14]) and high specific surface area (SSA) of nanoporous electrodes[15−18] makes these devices suitable for portable energy storage. The energy storage in EDLCs is achieved *via* a non-Faradaic mechanism, *i.e.*, due to the electrostatic interactions between the charged electrode surface and a couple nanometers thick layer of restructured electrolyte near the electrode surface.[19] Because this mechanism does not involve electrochemical redox reactions, the EDLCs have several key advantages compared to batteries, such as faster charging/discharging rate, higher delivered power, longer lifetime, and no susceptibility to overcharging. To date, the supercapacitors are commonly utilized in applications requiring short-time high power burst of energy, such as flash photography,[20] electric cars,[21] *etc.*

A key disadvantage of the current supercapacitors is their relatively low energy storage density. For example, the energy density stored by commercial EDLCs is about one order of magnitude less than in Li-ion batteries. Therefore, many recent experimental and theoretical research efforts in this field have focused on finding conceptually new approaches to design materials to increase the energy density in supercapacitors. As the non-Faradaic energy storage in EDLCs is achieved at the electrode−electrolyte interface,[22−25] designing electronically conductive porous materials with high SSA is considered as one of the main pathways to increase the energy density. Recent research demonstrated that it is possible to increase the SSA in porous materials from several hundred m^2/g, as observed for activated carbon[26] or powders,[27,28] to 2000−3000 m^2/g as

* Address correspondence to jenel.vatamanu@utah.edu, d.bedrov@utah.edu.

Received for review February 9, 2015 and accepted June 3, 2015.

Published online June 03, 2015
10.1021/acsnano.5b00945

reported for various C-fibers,[29−31] carbide-derived carbon,[32−35] aerogels,[36−38] and nanotubes.[39−44] Chen *et al.*[45] reported 4000 m^2/g SSA for rice-hull based carbon, Zhang and co-workers[46] synthesized C-based porous materials with good electronic conductivity and SSA as high as 3500−3900 m^2/g, while Farha *et al.*[47] showed that metallo-organic based frameworks can reach 7000 m^2/g SSA. Furthermore, the theoretically estimated upper limit for SSA is 14 000−26 000 m^2/g.[47,48] Therefore, the design of high SSA porous materials for supercapacitors remains one of the key routes for increasing the energy density in these devices.

Concomitant with the increase of SSA, a decrease in the pore widths to subnanometer size was also achieved. Intriguing new phenomena, such as an increase in capacitance, were discovered for tightly confined electrolytes in subnanometer pores.[49−55] For example, an experimental study by Largeot *et al.*[56] of capacitors comprised of RTIL electrolyte and carbide derived carbon (CDC) showed that the capacitance in subnanometer pores sharply increases by a factor of 2 as compared to the capacitance in wider pores or on open structure flat electrodes. In contrast, Centeno and co-workers, found almost no variation of the capacitance as a function of pore width, albeit using different nanostructured electrodes and electrolytes.[57−60] These earlier experimental observations triggered a number of theoretical investigations and prompted an interesting debate on the origin of this phenomenon. In this regard, several simulations[61−69] and analytical theories[70−76] have shown that the capacitance can be indeed enhanced due to ion confinement in tight nanopores; however, the extent of predicted enhancement remains debated.[64,73,74,77−80]

Several analytical models identified that the physical origin of the capacitance enhancement in nanopores is the screening[80−88] of electrostatic interactions between ions. As demonstrated by the Kondrat and Kornyshev[89] model, the polarization of conducting nanopore walls can screen out the electrostatic interactions between confined counterions (*i.e.*, the repulsion between ions of the same charge), allowing a denser ion packing (or "superionic states")[89] and therefore higher capacitances. While these models have established a qualitative understanding of the phenomena occurring inside the pores with ionic electrolytes, the understanding of correlations for chemically realistic systems as well as the quantitative comparison of experiments with simulation data is challenging for several reasons. First, so far a rather limited number of electrolytes and electrode structures have been investigated using chemically realistic models in molecular dynamics (MD) or Monte Carlo simulations. Often, the simulation studies are limited to one electrolyte, therefore making difficult to establish more generic correlations among the underlying chemical structure of ions, electrodes configuration and the resulting capacitances. Second, the quantitative comparison between experiments and modeling/simulations is often complicated by the variety of properties used to characterize the energy/charge storage in capacitors. In experimental works,[32,33,56] the capacitance enhancement observed in nanostructured supercapacitors was quantified using twice the integral capacitance (IC) for the entire device (IC_{cap}) measured at potential difference (ΔU) of about 2.5−3 V between electrodes, which is typically used in operation of the current generation of supercapacitors due to limitations in electrolyte electrochemical stability. In simulations, often systems with single electrode set up are used to minimize the computational cost. However, the contribution to the total capacitance from positive and negative electrodes can be quite asymmetric, and therefore, examination of $2IC_{cap}$ is a direct way to compare the extent of capacitance enhancement observed in nanostructured supercapacitors by experiments and simulations. The simulations, on the other hand, often report the differential capacitance (DC). Note that the IC is the ratio between the total charge density accumulated on the electrode divided by the applied potential, while the DC is the measure of the variation of the electrode charge due to small changes in applied potential. Thus, the DC dependence on the electrode potential provides important mechanistic insights into the processes occurring in the EDL during charging/discharging and can reach quite high values over a narrow range of potentials, particularly at low voltages or when abrupt changes in electrolyte composition occur due to co-ion expulsion from nanopores.[75,90−92] However, at high voltages the DC usually drops, and therefore large values of DC at low voltages do not necessarily lead to large overall IC at more elevated voltages preferred for energy storage.

The experimental study of Largeot *et al.*[56] using CDC nanoporous electrodes and a RTIL electrolyte showed that the $2IC_{cap}$ doubles from ~7 $\mu F/cm^2$ in mesoscale pores to 13.5 $\mu F/cm^2$ in subnanometer (0.7−0.8 nm wide) pores. To the best of our knowledge this phenomenon has not yet been quantitatively reproduced by simulations. Simulations based on coarse-grained models[90,91] or on the classical density functional theory[72,74,76] can predict large capacitances; however, these predictions are qualitative because many approximations and simplifications for the ion−ion and ion−surface interactions are used. Simulations with atomistically detailed force fields on the other hand, should provide a better quantitative assessment of the agreement between theory and experiment. However, previous simulations that showed IC up to ≈9.5−10 $\mu F/cm^2$ for electrolytes inside nanopores predicted the flat open surface electrode capacitances of ≈6.5−7 $\mu F/cm^2$; therefore, the relative enhancement in nanopores was limited to only 40−50%.[61,65] Also, our recent

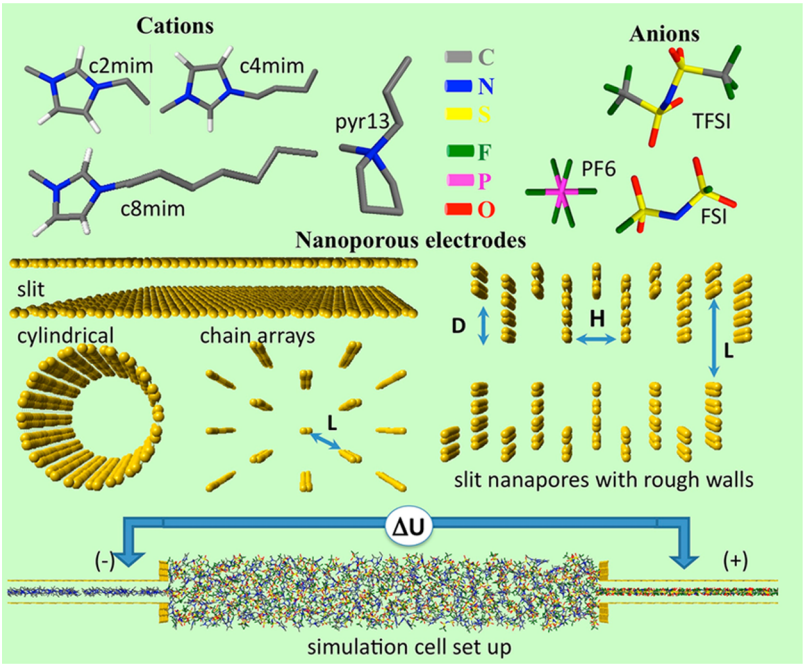

Scheme 1. Chemical structures of cations and anions comprising electrolytes, structures of nanoporous electrodes, and a snapshot of the simulation cell setup investigated in this work.

study of RTIL electrolytes in nanopores[87] predicted a similar extent of the relative enhancement in IC_{cap}. Therefore, previous simulations using chemically realistic models were not able to capture both the extent of the relative capacitance enhancement (*i.e.*, the ratio between IC_{cap}(nanopores) and IC_{cap}(flat open electrodes)) and the magnitude of the maximum capacitance $2IC_{cap}$ obtained for nanoporous electrodes in experiments.[56,93]

The apparent discrepancy between simulations and experimental observations indicates that the current understanding of the phenomena occurring with RTIL electrolytes inside charged nanoconfined environments may still be incomplete. Using advanced molecular simulation tools and chemically realistic force fields we have investigated a series of common RTIL electrolytes and a variety of nanoporous electrode structures in order to establish correlations between the variations in structural characteristics of components (*i.e.*, chemical structure of electrolyte ions, shape and width of nanopores, electrode surface roughness, *etc.*) and the resulting EDL capacitance. Analysis of these correlations and charge storage mechanisms allowed us to identify key phenomena contributing to the enhancement of charge storage in supercapacitors with nanostructured electrodes. This work also allowed us to determine key factors that lead to a capacitance enhancement and to rationalize a quantitative agreement of capacitances predicted from simulations with experimental data. Our results show that nanoconfinement and nanopore surface roughness are equally important for the capacitance enhancement and that their intrinsic dependence on the nanopore size must be carefully taken into account.

RESULTS AND DISCUSSIONS

In this work we have considered electrolytes comprised of several commonly utilized RTILs: 1-alkyl-3-methylimidazolium bis(trifluoromethylsulfonyl)imide ($[C_n$mim$][$TFSI$]$, $n = 2, 4, 8$), 1-ethyl-3-methylimidazolium salt of bis(fluoromethylsulfonyl)imide ($[C_2$mim$][$FSI$]$), 1-butyl-3-methylimidazolium hexafluorophosphate ($[C_4$mim$][PF_6]$) and *N*-propyl-*N*-methylpyrrolidinium bis(fluorosulfonyl)imide ($[pyr_{13}][$FSI$]$). The electrodes were comprised of carbon atoms and were considered purely conductive. For slit pore geometry with atomically flat surfaces the nanopore walls were represented using two graphene sheets. Cylindrical nanopores were represented using (n, m) carbon nanotubes with $n = m$ and values of n, m indices ranging from 6 to 15. Nanopores with atomically rough walls were represented as edge-exposed stack of graphene layers. By changing the offset in stacking of graphene layers we were able to manipulate with the extent of the nanopore surface roughness. Scheme 1 shows the chemical structure of cations and anions as well as illustrates the electrode structures used in this work.

Charge Storage in Slit Nanopores. We begin with the analysis of systems with symmetric electrodes containing slit nanopores that have identical widths and depths (*i.e.*, the volume accessible for electrolyte is the same on each electrode). In these systems the nanopore walls are comprised of atomically flat graphene layers. Since the charge storage by the capacitor is directly proportional to the IC and the applied

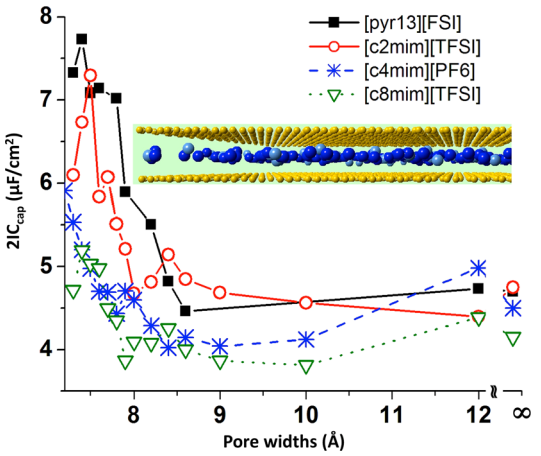

Figure 1. Total capacitance ($2IC_{cap}$) as a function of pore width as obtained from MD simulations for several RTILs and computed at ΔU = 3 V for all electrolytes except [pyr_{13}][TFSI], for which it was computed at 2.8 V.

potential we focus our analysis on examination of the capacitance dependence as a function of applied voltage.

Integral Capacitance versus Nanopore Width. First we summarize the influence of pore width on the EDL capacitance for several common RTILs inserted in slit pores. The pore widths varied from 7.3 to 12 Å. The potential difference between electrodes was set to 2.8 V. This particular value of the potential was chosen because it is sufficient to repel the co-ions from the nanopores (leaving inside the pores a counterion-rich phase) and it is within the electrochemical stability window for the majority of common RTILs. Pores tighter than 7.3 Å are less interesting from a practical viewpoint since most of the ions comprising common RTILs are too large to intercalate in such narrow pores. Pores wider than 12 Å show oscillations in capacitance dependence on pore width (the amplitudes of those oscillations are about ~10−15% compared to values on the flat surfaces)[60,72,91] and, hence, are not sufficient to significantly enhance the capacitance.[61,74,94] Therefore, we limit our study to nanopores widths below 1 nm where we expect to see a significant increase in capacitance.

Figure 1 shows the $2IC_{cap}$ as a function of the pore width for [pyr_{13}][FSI], [$C_n$mim][TFSI] n = 2, 4 and 8, and [C_4mim][PF_6] electrolytes obtained from our simulations. As the nanopore width decreases to ~9−10 Å there is a slight shallow minimum in capacitance, which is the signature of oscillatory dependence previously shown by analytical theories[72,73] and simulations.[61,64] Upon further reduction of the nanopore width a sharp increase of capacitance with a peak at width around 7.5 Å is observed showing a noticeable capacitance enhancement compared to values obtained for these RTILs on the basal plane graphite surfaces.[49,63,64] The largest relative capacitance enhancement was observed for the [pyr_{13}][FSI]

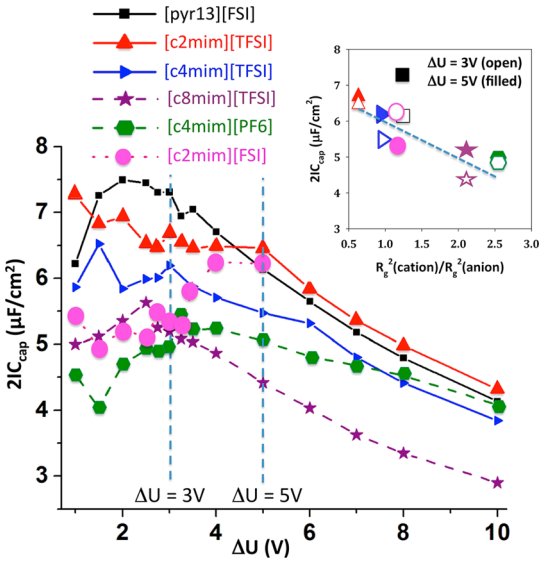

Figure 2. Dependence of the $2IC_{cap}$ for different electrolytes as a function of potential difference between electrodes (ΔU) containing symmetric 7.5 Å wide slit nanopores. The inset compares the $2IC_{cap}$ as a function of asymmetry in cation and anion sizes (measured by the ratio of calculated radii of gyration, see discussion in the text) compared for different electrolytes at two voltages, ΔU = 3 and 5 V.

(7.6 μF/cm^2 or 50% increase *vs* infinitely wide pore) followed by [C_2mim][TFSI] (7.0 μF/cm^2 or 40% increase *vs* infinitely wide pore). The [C_8mim][TFSI] RTIL containing cations with bulkier alkyl tails has generated a maximum of capacitance of 5.1 μF/cm^2, which is only 25% increase compared to a flat surface. The [C_4mim][PF_6], on the other hand, showed very small capacitance increase in the studied width range of slit nanopores. Although the capacitance dependencies on the nanopore width for slit pores obtained from simulations show a qualitative agreement with the experimental data that observed capacitance enhancement,[32,56] they clearly disagree quantitatively. The relative enhancement compared to open structure surfaces is only 50% in simulations while experiments report ~100% enhancement. Also the maximum value of $2IC_{cap}$ is around 7−8 μF/cm^2 in simulations, while experimental values are ~13 μF/cm^2. Taking into account that simulations (presented here as well as in the literature) of different RTILs generate qualitatively similar dependence of IC on pore dimensions, it is reasonable to conclude that the capacitance enhancement in nanopores with widths that are comparable to ions dimensions is largely independent of ions molecular details and therefore can be considered as a generic feature due to nanoconfinement.

Integral Capacitance versus Applied Potential. Next we examine the dependence of the total capacitance ($2IC_{cap}$) on the applied potential difference (ΔU). Figure 2 shows $2IC_{cap}$ for the slit nanopores having a width of 7.5 Å which, according to Figure 1, is an optimal dimension for most of the investigated RTILs. At low voltages (ΔU < 3 V) the capacitance either

slightly increases (*e.g.*, for $[C_4mim][PF_6]$) or stays constant. However, it begins to decrease monotonically (almost linearly) at higher voltages for all electrolytes. This capacitance decrease at higher voltages, where the nanopore is filled only with counterions (see discussion below), is due to compression (densification) of the counterions inside nanopores. The slope of the $2IC_{cap} = f(\Delta U)$ dependence at higher voltages is expected to correlate with the packing ability of counterions under external electric field. Indeed, Figure 2 shows that the decrease of $2IC_{cap}$ in the $\Delta U = 4$ to 10 V range is not sharp and it has rather similar slope for most RTILs except for $[C_4mim][PF_6]$. The observed weak dependence of the capacitance on ΔU (with an average slope of about 0.4−0.5(μF/cm^2)/V) implies that voltages even as high as 9−10 V do not saturate the nanopore with counterions and therefore still have relatively high values of capacitance. However, at $\Delta U > 7-8$ V the capacitance for most RTILs reaches the values corresponding to those observed on the flat basal plane graphite electrodes,[91,92] and therefore at these high voltages, the nanoconfinement of electrolyte does not provide any capacitance enhancement.

The comparison of capacitances for different electrolytes shown in Figure 2 raises an obvious question: how the observed trend correlates with the cation/anion size asymmetry? To address this issue we have estimated ion sizes by computing an effective "radius of gyration" (R_g) for each ion in bulk electrolyte. In this calculation we used the location of atoms centers and the corresponding atomic masses to calculate the center-of-mass position and an effective R_g of the ions. While for such small molecules the spherical symmetry might not be the best approximation of ion dimensions, the R_g should capture the trend in ions' relative sizes. For the cations the following order of R_g^2 has been obtained: C_2mim (4.25 Å^2) < pyr_{13} (4.46 Å^2) < C_4mim (6.44 Å^2) < C_8mim (14.15 Å^2), while for the anions: PF_6 (2.53 Å^2) < FSI (3.62 Å^2) < TFSI (6.69 Å^2). Using these values the extent of asymmetry of cation and anion volumes comprising a given RTIL electrolyte can be defined as R_g^2(cation)/R_g^2(anion). The inset in Figure 2 shows the IC_{cap} as a function of R_g^2(cation)/R_g^2(anion) at 3 and 5 V for several electrolytes inside the 7.5 Å wide nanopore. While there is some scatter in the data, a generic trend can be observed: the larger the asymmetry in cation/anion size, the lower the capacitance. RTILs with relatively similar size cations and anions (*e.g.*, $[pyr_{13}][FSI]$ or $[C_2mim][TFSI]$) have systematically higher capacitance compared to RTILs with more asymmetric ion volumes (*e.g.*, $[C_4mim][PF_6]$ or $[C_8mim][TFSI]$). The difference in capacitance between two electrolytes can be as much as 2 μF/cm^2 indicating that tuning the electrolyte chemical structure for a given nanopore size and geometry can lead to a capacitance increase of as much as 50%, which is significant. This is comparable to the extent of the capacitance enhancement obtained by changing the nanopore width in our simulations of atomically smooth slit pores discussed above.

Differential Capacitance. A further insight into the mechanisms of charge accumulation as a function of electrode potential can be gained from examining the shape of the differential capacitance (DC) *versus* the electrode potential. The DC was computed for several RTILs inside 7.5 Å wide nanopores and is shown in Figure 3. Panels 3a−c show that the RTILs based on $C_n$mim cations (n = 2, 4, 8) have qualitative similar dependences of DC, *i.e.*, a camel-shaped DC with a minimum near potential of zero charge (PZC) and two maxima at higher voltages. We would like to point out that the observed dependences of DC are noticeably different from those generated by open structure flat surfaces that showed almost no dependence on voltage.[95] The U-shaped minimum at lower voltages is very pronounced. In contrast, the $[pyr_{13}][FSI]$ generated an overall bell-shape DC with a broad maximum near PZC followed by an abrupt decrease of DC at electrode potentials of about ±2 V (see Figure 3d). The difference in the behavior between $C_n$mim- and pyr_{13}-based electrolytes is related to the difference in the mechanisms of electrolyte composition change inside the pore upon charging. RTILs containing $C_n$mim cations showed an abrupt expulsion of co-ions from the nanopore leading to sharp changes in ion composition and densities inside the pore (see discussion below) with increasing voltage. In $[pyr_{13}][FSI]$, on the other hand, the charge separation inside nanopores was occurring through monotonic swapping of ions and smooth change in composition with increasing voltage. Similar phase transitions inside nanopores were previously predicted and discussed by Kiyohara *et al.*[96,97] and by Kondrat *et al.*[89] in their modeling of systems comprised of spherical ions. In the case of the Kiyohara−Sugino−Asaka[97] transition, a pore empty at PZC (not wetted by electrolyte) is abruptly filled with counterions after electrode voltage exceeds some larger value. In contrast, in the Kondrat−Kornyshev[89] transition, the nanopore is initially wetted by electrolyte and is filled with both ions at PZC. As the potential increases then at some larger voltage, the co-ions are abruptly expelled from the nanopore (*i.e.*, cations and anions are demixing). Our study shows that the chemical structure of RTILs plays an important role in determining what type of transition occurs inside the nanopore. Specifically, the RTILs based on the $C_n$mim cations show a Kondrat−Kornyshev[89] transition, while $[pyr_{13}][FSI]$ RTIL shows a continuous (albeit at some voltages a relatively sharp) change in ion composition inside nanopore as a function of the electrode potential, which is similar to that observed by Kondrat *et al.* using Monte Carlo simulations.[90] Although not observed for the pores studied here, the Kiyohara−Sugino−Asaka[97] type of transition is expected to occur

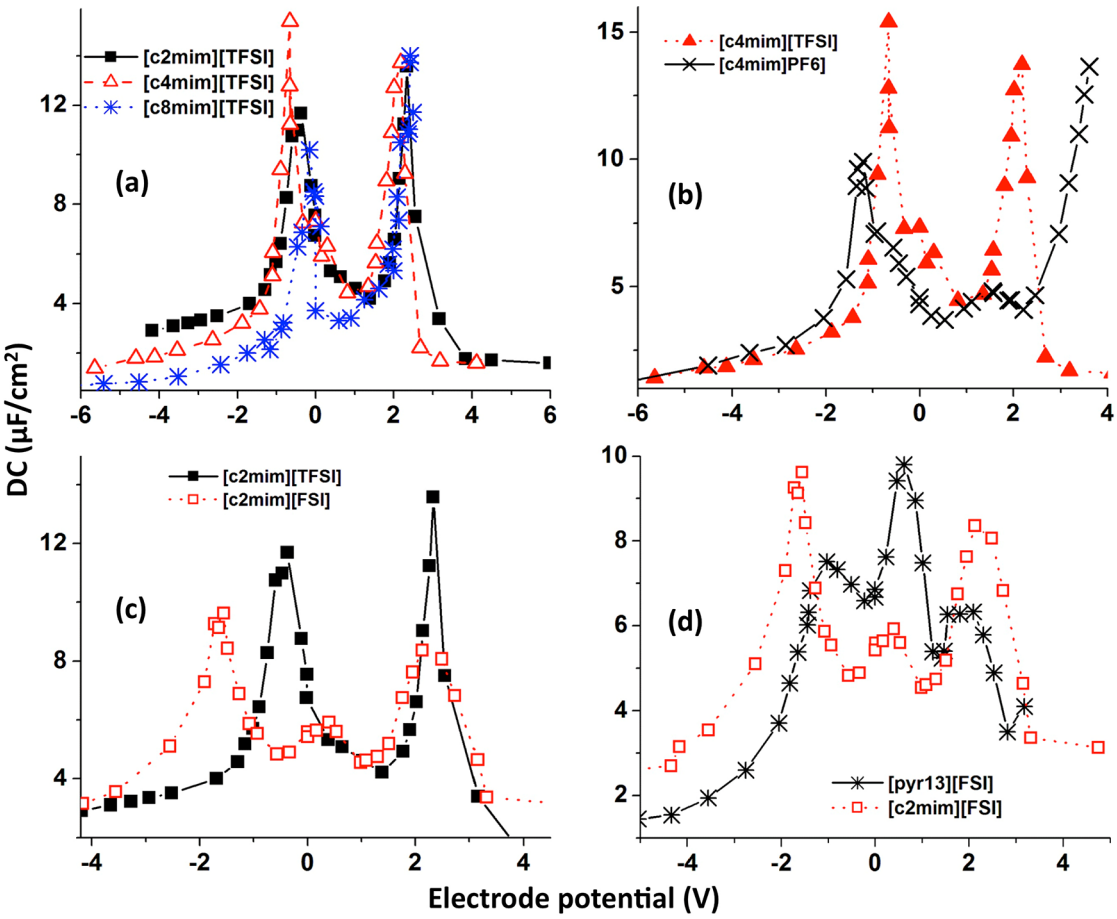

Figure 3. Differential capacitance as a function of electrode potential for various electrolytes inserted in slit pores with 7.5 Å width.

if the nanopore dimensions are reduced even further, hence increasing the steric repulsion of the ions by the nanopore walls, or if the nanopore walls are chemically modified such that it reduces the favorable interaction with electrolyte and leads to dry pores at PZC. For example, in some systems containing 1D-chain arrays we have observed such behavior on negative electrodes when the spacing between the chains was smaller than 7 Å.

For RTILs with TFSI anion we have compared several $C_n$mim cations (Figure 3a) with different length of the alkyl tails. Electrolytes with ions having longer alkyl tails are of practical interest due to their lower freezing or vitrification point inside the nanopore.[98] Therefore, while increasing the length of the alkyl tail can reduce the capacitance as well as increase their viscosity, which is detrimental to the fast charging/discharging rates, these electrolytes might have an advantage for applications at lower temperatures. The increase of the cation alkyl tail decreases the overall DC (and IC) because of (i) the excluded volume effect (the more voluminous cation with longer alkyl tail results in the packing of fewer ions inside the nanopores and (ii) the increasing asymmetry between cations and anions in symmetric nanopores can lead to a mismatch in the capacitance enhancement on individual electrodes and, hence, to a lower total capacitance. However, aside from the systematic lowering of DC, the increase of $C_n$mim alkyl tail does not have a dramatic effect on the overall shape of DC. This behavior can be rationalized by the fact that mostly nonpolar alkyl groups do not polarize the electrode surface and cannot contribute to the charge storage, *i.e.*, their main contribution inside the pore is an excluded volume effect.[99] Therefore, at PZC, the actual density of ionic groups at the nanopore surface is relatively small, but as the electrode potential increases, the ionic groups replace the alkyl tails on the surface and hence, the overall density of ions (and DC) is increasing.

For the $C_n$mim-based RTILs the broadness of the minimum (or the separation between voltages corresponding to DC maxima) depends on the anion structure. For example, for [C_4mim][TFSI] we observe the maxima in DC at −1.5 V and +2 V. Replacing TFSI anion with a smaller PF_6 increases the potential spread between the maxima at −1.8 V and +2.5 V (see Figure 3b). Similarly, in the [C_2mim][FSI] the potential for the maximum on the negative electrode is shifted by almost −1 V compared to that in [C_2mim][TFSI] electrolyte (see Figure 3c). Note that these pronounced

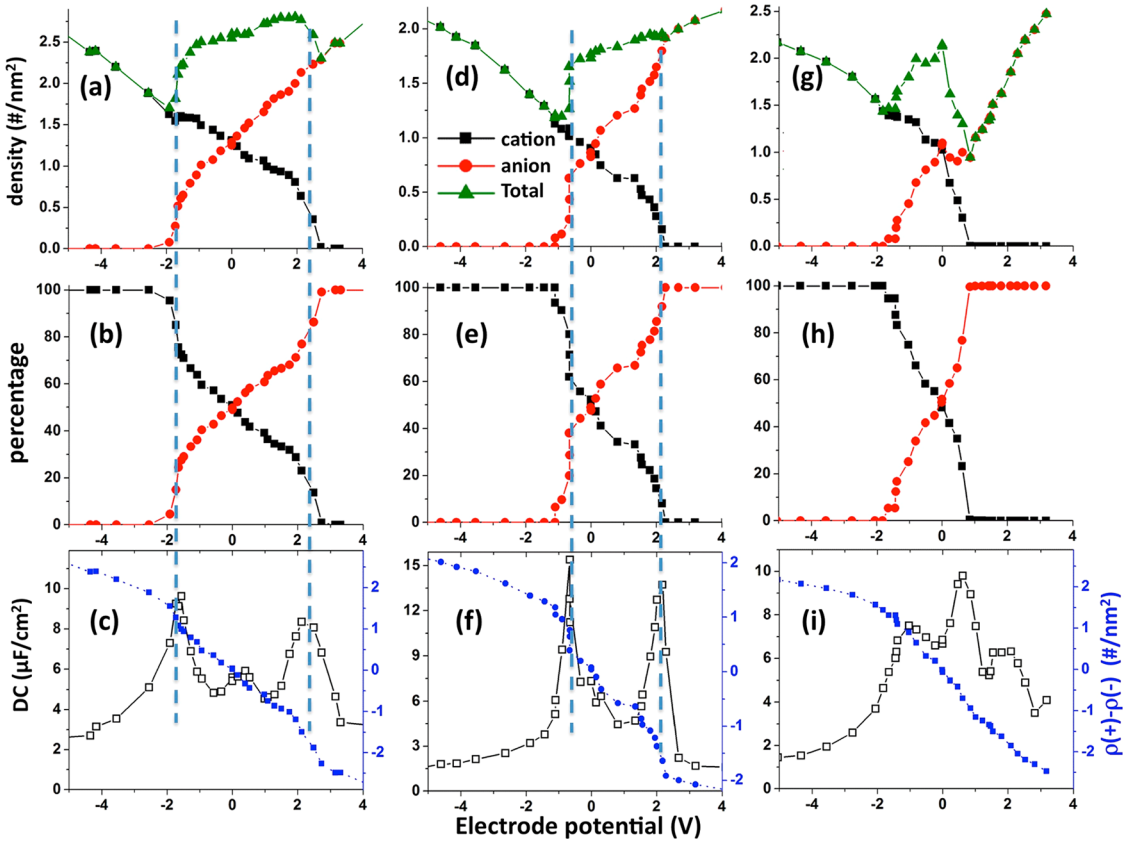

Figure 4. Ion densities inside nanopore (upper horizontal panels a,d,g), percentage of ions inside nanopore (middle horizontal panels b,e,h) and DC as well as the total excess charge inside nanopore (bottom panels c,f,i) as a function of electrode potential. The left column (a,b,c) are for [C_2mim][FSI], the middle column (d,e,f) are for [C_4mim][TFSI], and the right column (g,h,i) are for [pyr_{13}][FSI] electrolytes. All data are from systems symmetric electrodes with 7.5 Å wide slit nanopores.

maxima in DC are only observed in the narrow, sub-nanometer size pores. In wider pores (*e.g.*, 12 Å wide), the DC *vs* the electrode potential is almost featureless and shows only a weak dependence on the electrode potential.[92] Hence, the peaks in DC shown in Figure 3 are primarily responsible for the total capacitance enhancement (shown in Figure 1) upon reduction of nanopore dimensions. However, the mismatch in the location of these peaks on the negative and positive electrodes means that for a fixed potential difference ΔU it is unlikely that both peaks in DC will be included (assuming values of $\Delta U \sim 3-4$ V that are typically used in practice), and hence, the capacitance enhancement will be only coming from one of the electrodes. For example, lets consider Figure 3a and assume $\Delta U = 3$ V with approximately symmetric potentials of ± 1.5 V on each electrode. For [$C_n$mim][TFSI] RTILs this range of electrode potentials on the negative side includes the entire peak in DC, and therefore, the negative electrode shows strong contribution to the integral capacitance enhancement. However, on the positive electrode, the DC peak is outside of this range of electrode potential (the peak is located in the 1.5−3 V range) leading to no enhancement of the capacitance on the positive electrode for these RTILs at $\Delta U = 3$ V. Therefore, even if on the negative electrode the applied ΔU results in an increase of IC^- by a factor of 2, because the total capacitance of the cell is defined as $1/IC_{cap} = 1/IC^+ + 1/IC^-$, the increase in the IC_{cap} will only be ~33% as the IC^+ is not increasing. In order to obtain the capacitance enhancement from both electrodes and to maximize the IC_{cap} for RTILs shown in Figure 3a, a $\Delta U \sim 6$ V that would include both peaks in DC is necessary. However, such large voltage might be outside of the electrochemical stability of [$C_n$mim][TFSI].

Mechanism for Capacitance Enhancement in Narrow Nanopores. In order to understand the shape of the DC dependence on the electrode potential we have analyzed the change in ion density and the composition inside the nanopores as a function of the electrode potential. Figure 4 shows the ions density inside the 7.5 Å wide nanopore as a function of electrode potential for [C_2mim][FSI] (left column), [C_4mim][TFSI] (middle column), and [pyr_{13}][FSI] (right column). The top row of panels shows the average density of each ion type as well as the total density of both ion types inside nanopore. At PZC the total density of ions is reasonably high indicating that these electrolytes show good wetability of the nanopore in the uncharged state. As the magnitude of the electrode potential increases, two regimes can be distinguished: (1) a potential window where a swapping of co-ions and counterions

occurs upon changing the voltage, and (2) after the complete expulsion of co-ions from the nanopore, a densification of counterions is observed upon further increase of electrode potential magnitude. Depending on the chemical structure of the electrolyte, the counterion/co-ion swapping can have either a monotonic (*i.e.*, almost linear) dependence on voltage, as it is in the case of [pyr_{13}][FSI], or it can have a more abrupt dependence with a sharp depletion of co-ions upon small changes in voltage (*e.g.*, as observed for [C_2mim][FSI] and [C_4mim][TFSI]). Note that in most systems, the total density of ions is decreasing during the co-ion expulsion process (see Figure 4a,d,g) and only after the co-ions have been completely expelled from nanopores, the total ion density begins to increase again and eventually reaches values that are higher than initial values near PZC. The abrupt changes in ion density and composition inside charged nanopores have been discussed in more detail in previous works.[65,89,92,96,97]

The discussed above changes in ion density and composition inside nanopores are strongly correlated with the features observed in DC. Figures 4c,f,i show the corresponding DC and the deviation of the total electrolyte charge density (from its value at PZC) inside the nanopore as a function of electrode potential. The observed strong peaks in DC for [C_2mim][FSI] and [C_4mim][TFSI] coincide with the voltages where a sharp co-ion demixing from counterions and their expulsion from nanopore is observed (marked by vertical lines). In the [pyr_{13}][FSI] electrolyte, however, the absence of such abrupt changes in electrolyte composition inside nanopore is consistent with the relatively broad, bell-shape DC behavior near PZC. It is then interesting to analyze how the voltage at which the abrupt change in electrolyte composition is observed (due to co-ion expelling) depends on the electrolyte chemical structure. For example, the comparison of [C_2mim][FSI] (Figure 4a,b,c) and [pyr_{13}][FSI] (Figure 4g,h,i) shows that complete expulsion of the FSI anion occurs approximately at the same electrode potential of -1.9 V, yet on the positive electrode it takes only $+0.9$ V to deplete the pyr_{13} cation from the nanopore while it takes $+2.3$ V to remove the C_2mim co-ion. In the [C_2mim][TFSI] and [C_2mim][FSI] the co-ion expulsion on the positive electrode occurs approximately at the same voltage while on the negative electrode they are different by $\sim$1 V. This illustrates that while the counterion is the dominant component of the electrolyte inside the charged nanopore, the chemical structure of the co-ion (*i.e.*, the minority component) significantly affects the co-ion expelling process and, hence, the location of peaks in DC. Of course, in systems with co-ions of significantly different shape and size (*e.g.*, TFSI *vs* PF_6 anions), the ability of the counterion to pack inside the nanopore will also influence the DC (compare DC on the positive electrode for [C_4mim][TFSI] and [C_4mim][PF_6], Figure 3b).

Slit Nanopores with Asymmetric Volumes. The results reported above for the symmetric slit nanopores indicate that due to the asymmetry in the co-ion and counterion chemical structure (*i.e.*, the ions' shape, size, and charge distribution) the maxima in DC occur at different voltages on the positive and negative electrodes and therefore, it is hard to expect the capacitance enhancement (inside narrow nanopores) to occur at equivalent magnitudes of electrode voltages on both electrodes. The symmetric electrode setup might not be optimal for ions with asymmetric shapes and volumes as the less voluminous ions are likely to require less space inside the charged nanopore than its larger counterion. Indeed, Figure 2 shows that RTILs with more asymmetry in ion sizes generated smaller capacitances. On the other hand, these ions also have very different geometry and molecular charge distributions, and therefore, the question is whether this tendency is simply related to the ion volume asymmetry and to the fact that in symmetric nanopores there is too much volume provided for the less voluminous counterion. In other words, can the capacitance be further enhanced by manipulating with nanopore volumes on the positive and negative electrodes to offset the asymmetry in the volumes of cation and anion comprising electrolyte?

To investigate this we have set slit nanopore electrodes with a different ratio of volumes accessible for electrolyte in the positive and negative pores (V^-/V^+). In this set up we kept the width of the nanopore the same (7.5 Å) but changed the depth of one of the nanopores to allow the desired V^-/V^+ ratio. The assumption in this approach is that the charge conservation requires that the total amount of charge accumulated in the positive pore is equal and opposite in sign to the total charge in the negative pore. Therefore, the composition inside the nanopore on one electrode is not independent from the electrolyte composition on the opposite electrode. In the nanopore with smaller counterion there is enough free volume that can accommodate extra cation/anion pairs. These extra cation/anion pairs do not change the amount of accumulated charge but the presence of few additional co-ions can reduce the repulsive interactions between counterions (which are in excess). Therefore, by reducing the volume of the nanopore containing smaller counterions we provide less volume for these counterions (*e.g.*, FSI anion in [pyr_{13}][FSI] electrolyte inside the positive nanopore) which can lead to co-ion expulsion from the pore at lower voltages and either increase the value of DC or shift the peak in DC closer to PZC.

Figure 5 shows the density of ions and fraction of counterions for [C_8mim][TFSI] inside the negative and positive (7.5 Å wide) nanopores with asymmetric V^-/V^+ ratio of volumes as a function of applied potential differences. As we discussed above the C_8mim cation is

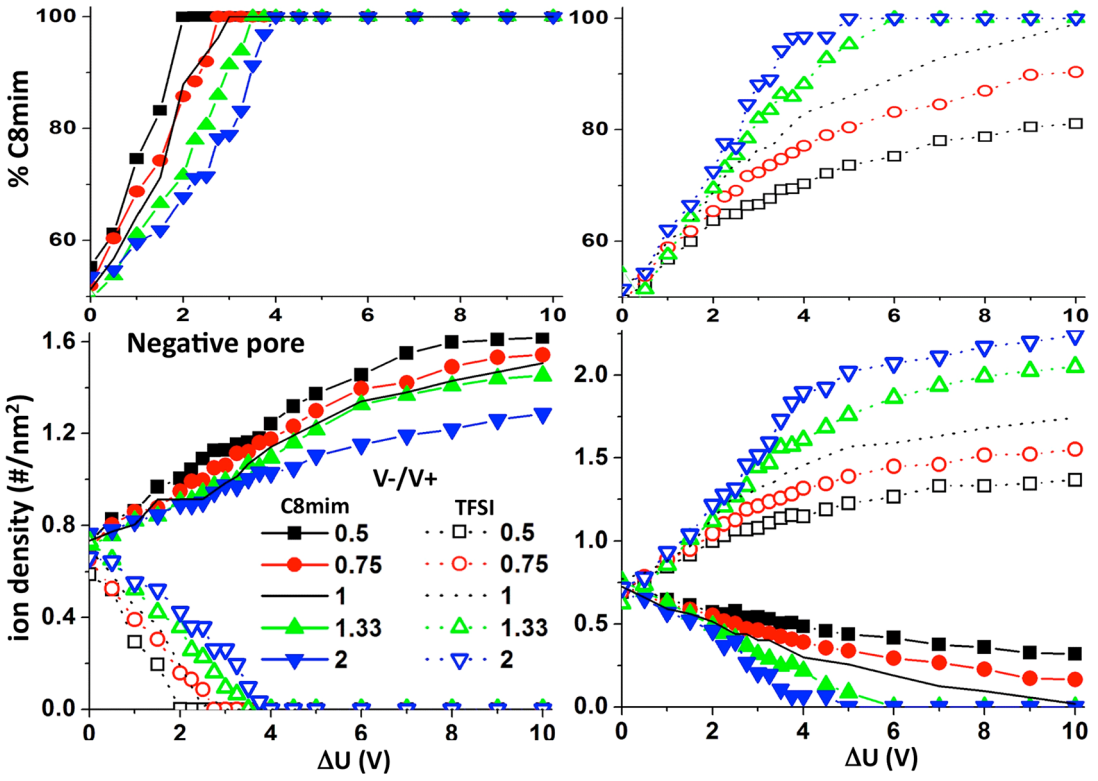

Figure 5. Average density of ions in [C_8mim][TFSI] and the fraction of counterions inside the 7.5 Å wide negative (left panels) and positive (right panels) nanopores with asymmetric volumes as a function of applied potential difference.

noticeably larger than TFSI anion and hence, this electrolyte can be a good case for testing the correlations between cation/anion and positive/negative pore volume asymmetries. As we can see from Figure 5 the asymmetry in nanopore volumes certainly makes influence on the counterion packing. For example, left panels show the data for the negative nanopore in which the C_8mim cation is the counterion. If this pore volume is smaller than the volume of the positive nanopore (*e.g.*, $V^-/V^+ = 0.5$) it allows to accumulate more C_8mim counterions per surface area of the pore compared to the symmetric nanopore case ($V^-/V^+ = 1.0$). Also the co-ion expulsion from nanopores occurs at lower voltages (see top panels which show the percentage of the counterions inside the nanopore). However, on the positive pore the same ratio of nanopore volumes causes an opposite effect: the density of TFSI anions is decreasing inside the nanopore, and the co-ion expulsion from the pore is shifted to higher voltages. If the ratio of nanopore volumes is reversed then an opposite effect is observed.

The trends in Figure 5 show that favorable effects inside one nanopore (*i.e.*, the increase of counterion density and lower potentials for co-ion expulsion) are offset by unfavorable changes on the other electrode when the asymmetry in volumes of electrode nanopores is introduced. Then the question is can this effect be used to further enhance the capacitance? More detailed examination of Figure 5 shows some promise. For example, for $V^-/V^+ = 2.0$ at $\Delta U = 3$ V the drop in the density of the C_8mim ions in the negative pore is less than 0.1 #/nm^2 compared to symmetric slit pores. Yet, the increase of TFSI density in the positive nanopore at the same voltage is about 0.2 #/nm^2. Therefore, it is possible that the total capacitance will have some enhancement. Indeed, Figure 6a supports this supposition and shows the total capacitance for the [C_8mim][TFSI] electrolyte in electrodes with 7.5 Å wide pores with different V^-/V^+ ratios. At low voltages the influence of V^-/V^+ is not obvious; however, at $\Delta U >$ 2.5 V a clear trend is emerging. Systems with large volumes for the negative pores ($V^-/V^+ > 1.0$) show systematically higher capacitance compared to symmetric case, while systems with $V^-/V^+ < 1.0$ show a noticeable drop in the capacitance. For example, at the potential difference of 3.75 V the IC increases from 4 μF/cm^2 for $V^-/V^+ = 0.5$ to ~5.3 μF/cm^2 for $V^-/V^+ = 2$, which is about 30% increase in capacitance. This trend is consistent with the above-discussed mechanism. Systems with a larger negative nanopore volume (compared to positive nanopore volume) allow to compensate the corresponding counterion size difference and hence to increase the overall number of ions intercalating inside nanopores at a given applied voltage. However, for electrolytes comprised of similar size ions, such as *e.g.*, [pyr_{13}][FSI], the deviation from symmetric volumes for the positive and negative nanopores would likely lead to either a negligible

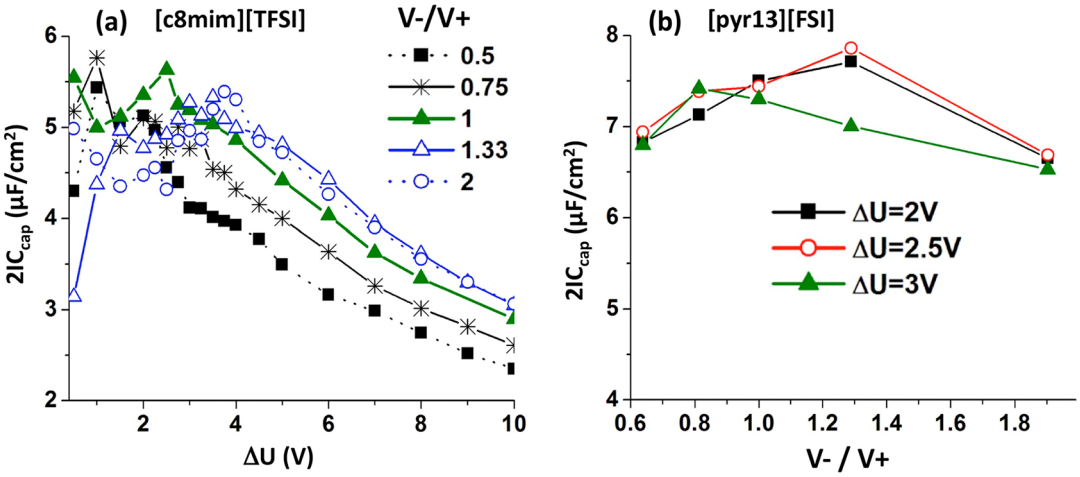

Figure 6. (a) The dependence of $2IC_{cap}$ on voltage and on the ratio between the available volume of the negative and positive nanopores for $[C_8mim][TFSI]$ electrolyte. (b) The dependence of $2IC_{cap}$ on the ratio between the available volume of the positive and negative pore for $[pyr_{13}][FSI]$ electrolyte for an asymmetric electrode setup where the available nanopore volumes on the positive and negative electrode were not equal. The integral capacitances were computed at three voltages.

change or a reduction of the total capacitance. Figure 6b shows the total capacitance for the $[pyr_{13}][FSI]$ at different voltages as a function of V^-/V^+. While there is some small enhancement at low voltages and small volume asymmetry, overall the deviation from $V^-/V^+ = 1.0$ ratio in either direction leads to reduction of the capacitance.

The observed trends for nanopores with asymmetric volumes have an important consequence. The electrolyte composition and density inside nanopores on one of the electrodes is not independent from the electrolyte structure and composition on the other electrode. The composition of the inserted electrolyte is not only determined by the cation−anion and the electrode−electrolyte interactions, but also by the ratio of accessible (for electrolyte) volumes available inside nanopores on both electrodes. This means that the optimization of the total capacitance of the capacitor requires tuning of both the (positive and negative) electrodes and the electrolyte at the same time such that the available nanopore volumes on each individual electrode are corresponding to the "excluded volumes" of the counterions inside nanopores.

The Role of Electrolyte Nanoconfinement in the Capacitance Enhancement. All simulations of slit nanopores discussed above showed a total capacitance of up to 8 $\mu F/cm^2$ (or <50% enhancement compared to infinitely wide pore). Yet, experimental works have reported values of ~13 $\mu F/cm^2$ (or >100% enhancement relative to the infinitely wide pore) for typical RTILs.[31,33,49,56] If the screening of ion interactions due to the nanopore wall polarization and the consequent denser packing of counterions inside slit nanopores (superionic states)[89] was the only driving force for the capacitance enhancement, the simulation predictions should be consistent with the observed experimental data. In order to achieve 13 $\mu F/cm^2$ at 2.5 V, a charge density on the nanopore surface of about $1e/nm^2$ would be required. To generate such surface charge density the inserted layer should contain a counterion excess density of ~2 $ions/nm^2$. However, as shown in Figure 4c,d,i to achieve these values of excess charge typically requires a driving force corresponding to $\Delta U > 6$ V. The impossibility of reaching 13 $\mu F/cm^2$ (purely non-Faradaic) for $\Delta U \sim 2.5-3$ V in atomically flat slit nanopores for typical RTILs can be further understood from the dependence of the individual and total densities of ions on applied voltage. Figure 4 upper panels show that near PZC, as the electrode potential values increase, the total density of ions often decreases (by as much as ~25−30%) upon reaching the voltage where the co-ions are expelled. Therefore, at $\Delta U \sim 2.5-3$ V the typical excess density of counterions inside the nanopores is on the order 1.0−1.2 $ions/nm^2$, which is not large enough to generate the required countercharge for the 13 $\mu F/cm^2$ capacitance observed in experiments. Figure 4 also shows that after the expulsion of co-ions, the densification of the counterions inside nanopores with increasing the potential difference has almost a linear dependence with a relatively small slope.

The decrease of the total density at the phase transition voltage is important because it implies that although an extra free space is created due to co-ion leaving the pore, this space is not refilled by counterions at these voltages. In other words, the screening of electrostatic repulsion between counterions by the conductive nanopore walls is only strong enough to maintain elevated (or only slightly increased) densities of counterions, but it is not strong enough to allow refilling of all available space created by co-ion expulsion. Then it is not surprising to observe that the counterion condensation mechanism responsible for

the charge accumulation at voltages above co-ion expulsion (*i.e.*, $\Delta U > 4$ V) is a slow (*vs* potential) process leading to a monotonic decrease of capacitance with a rate of $\approx 0.4-0.5(\mu F/cm^2)/V$ as the voltage increases up to 10 V (see Figure 2). The Superionic states predicted by the Kondrat and Kornyshev model,[89] consisting of densely packed counterions with the density close to the packing limit, are possible in realistic RTILs. However, to reach the packing limit for the systems studied here, larger voltages that, are likely to be above the electrochemical stability, are needed. For all electrolytes studied here inside the atomically flat slit pores, the key mechanism to enhance the capacitance is the sharp expulsion of co-ions from nanopore at low (ΔU = 2−3 V) voltages. However, this process of electrolyte composition change alone (without additional counterion condensation) only generates ~50% of relative enhancement of capacitance or ICs up to 7−8 $\mu F/cm^2$ at the co-ion expulsion potential (of about 2−3 V). Therefore, we conclude that regular slit nanopores with atomically flat walls cannot generate capacitances comparable to experimental values (of around 13 $\mu F/cm^2$) for realistic RTIL electrolytes.

Influence of Nanopore Structure on Increasing the Capacitances. The inability of the simulations using slit pore geometries and electrolyte nanoconfinement effect to reproduce the values and the extent of the capacitance enhancement observed in experiments brings the following question: are there any additional contributions to the capacitance enhancement in realistic systems that were not previously considered? There are a number of factors that can contribute and are not considered by our classical simulations. For example, the electrode surfaces can contain dopants that change the quantum capacitance of the electrode material, or various electrochemical (Faradaic) processes at electrolyte-electrode interface can be contributing to the capacitance. However, the influence of these factors is outside of the scope of this work. What we want to address here is whether it is possible to achieve experimental values of capacitance based on conducting pores only. Experimentally investigated carbon-based nanoporous electrodes have a much more complex morphology of nanopores and surface structure than we have considered in our simulations using slit geometry with atomically flat surfaces. For example, the CDC or activated carbons have a variety of structural elements such as curved surfaces and atomic scale roughness due to exposed edges and even short strands of single carbon chains (carbynes).[100] All these structural motifs can influence the EDL structure and the charge storage capabilities as it has been shown previously in our works for open structures (*i.e.*, electrode surfaces exposed to bulk electrolyte).[100] Below we will investigate the influence of these structural characteristics on EDL capacitance

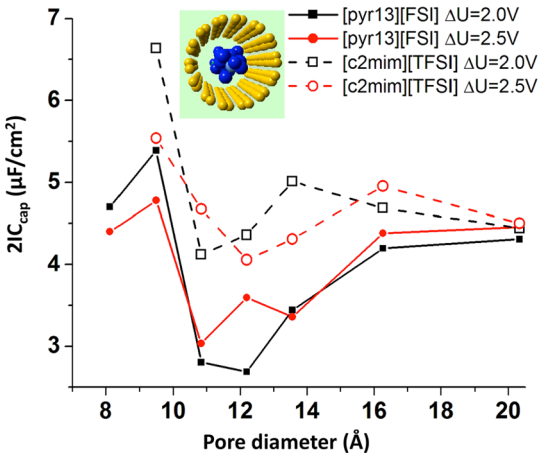

Figure 7. Dependence of $2IC_{cap}$ on the diameter of cylindrical nanopore obtained for two RTILs at two different applied voltages.

inside nanopores, therefore combining the electrolyte nanoconfinement effect with curvature and surface roughness of electrode nanopores.

Cylindrical Nanopore. First we examine the influence of curvature on the capacitance. Specifically, we investigated the capacitance generated by insertion of $[pyr_{13}][FSI]$ and $[C_2mim][TFSI]$ electrolytes inside carbon nanotubes. The nanopores were represented by (6,6), (7,7), (8,8), (9,9), (10,10), (12,12) and (15,15) carbon single wall nanotubes with corresponding diameters of 8.1, 9.49, 10.84, 12.2, 13.56 and 20.34 Å, respectively. Figure 7 shows the $2IC_{cap}$ as a function of nanotube diameter for ΔU = 2 and 2.5 V. The pores were loaded symmetrically; *i.e.*, the positive and the negative pores had equal pore diameters and equal volume accessible to electrolyte. Interestingly, in contrast to observations in slit pores, inside nanotube pores the $[pyr_{13}][FSI]$ generated slightly smaller capacitances than the $[C_2mim][TFSI]$ indicating that pore geometry plays a role in defining the capacitance enhancement. In fact, the $[pyr_{13}][FSI]$ electrolyte barely shows any capacitance enhancement upon reduction of the nanotube diameter. For $[C_2mim][TFSI]$ we observe qualitatively similar behavior as in slit nanopores, *i.e.*, a capacitance enhancement for pore diameters that are comparable to ions dimensions. The enhancement occurred at the applied potentials where the counterions and co-ions almost completely separate during the insertion into the pore generating a confined electrolyte phase rich in counterions. The overall capacitances (normalized per surface area) are slightly smaller in the cylindrical pores than in slit pores of similar widths (as expected from simple steric considerations for these bulkier ions), however, the magnitudes of capacitance are similar, *i.e.*, around 5−7 $\mu F/cm^2$, which is still noticeably lower than the experimental values for typical nanoporous carbon-based electrodes. Note that if the capacitance is calculated per volume accessible for electrolyte inside the nanopore, the cylindrical pores

generate systematically larger capacitance compared to slit pore geometry due to intrinsic difference in surface to volume ratio for these geometries.

Slit Nanopores with Rough Surfaces. Next we investigate the capacitance enhancement in nanopores with atomically rough surfaces. Previously we showed that nanopatterning of electrode surfaces with atomically rough textures of dimensions comparable to ions' size can generate capacitances that are about 50% larger than the capacitance on atomically flat surfaces.[101−103] Similar effect of surface roughness was recently observed for ionic solutions by Ho *et al.*[104] We previously showed that the rough edges promote large local electrostatic fields near the electrode surface. These local fields facilitate the ion separation in the EDL at lower voltages, which leads to higher capacitances.[102] Therefore, here we explore the combined effect of pore surface roughness and nanoconfinement on the capacitance enhancement for $[pyr_{13}][FSI]$ and $[C_2mim][TFSI]$ electrolytes. For this study the rough pore was built from two prismatic faces of graphite having a depth of the surface pattern D = 5.1 Å and a distance H = 7.3 Å between graphene planes comprising grooves (see Scheme 1). This particular surface topography was chosen based on our previous investigations[102] that showed significant increase of IC for this surface pattern exposed to bulk electrolytes (*i.e.*, open structures).

Figure 8 shows the $2IC_{cap}$ for $[C_2mim][TFSI]$ as a function of the nanopore width (L) for ΔU = 2, 2.5, and 3 V. The dependence of the capacitance on the nanopore width for atomically rough pores is qualitatively similar to that of the smooth slit pores, specifically: (i) it has a maximum at small width, (ii) it has a minimum for pore widths between 12 and 14 Å, and (iii) it remains almost constant for larger separations. The increase in capacitance in narrow pores again strongly coincides with the co-ion expulsion from nanopores. However, the nanopores with rough surfaces require lower voltages to expel the co-ions from the pores. The maximum $2IC_{cap}$ of 11.4 μF/cm^2 was observed at ΔU = 2 V decreasing to ~10 μF/cm^2 at ΔU = 2.5 V and 9 μF/cm^2 at ΔU = 3 V. Also the maximum of IC is broader (*i.e.*, it is extended over ~2 Å) than it is the case for flat (slit) pores. The $[pyr_{13}][FSI]$ electrolyte was investigated only at one pore width (L = 10.4 Å) and has generated capacitance of ~9 μF/cm^2 at all three voltages suggesting that the particular pore/surface pattern geometry might not be the optimal for this electrolyte.

In order to understand why the nanopores with rough surfaces generate larger capacitances than those with flat surfaces, we compare the ionic density and the composition of $[C_2mim][TFSI]$ inserted in the optimal slit and in rough pores. We found that the mechanism of the capacitance enhancement (ion separation *versus* densification) can be voltage dependent as shown above. For the rough geometry at a

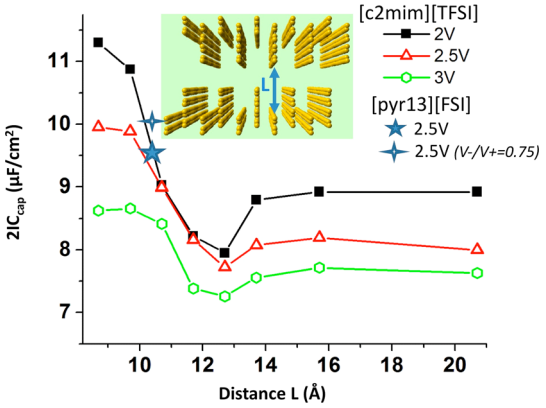

Figure 8. Dependence of $2IC_{cap}$ on nanopore width (L) for ΔU = 2, 2.5, and 3 V for $[C_2mim][TFSI]$ inside atomically rough nanopores.

potential difference between electrodes of 2 V, both the positive and the negative pore generate a total layer density of 1.36 ions/nm^2 containing >99% counterions. In contrast, in the nanopore with flat walls there are still 20% of co-ions in the negative pore and 30% of co-ions in the positive pore at this voltage. The counterion excess density is 0.86 ions/nm^2. However, at ΔU = 2 V the total electrolyte density was larger in the slit pores than in the rough ones. The latter is due to the presence of co-ions that can screen out the repulsion between counterions and allowing overall denser packing of ions. Therefore, at 2 V the enhancement in capacitance in rough pores (*vs* smooth flat pore geometry) comes primarily from a better separation of counterions triggered by the rough edges of nanopore walls rather than from the additional densification of the electrolyte. At ΔU = 3 V however, the screening becomes sufficiently strong to separate (almost) completely the counterions in both slit and rough nanopores and to condense the counterions. The total density at ΔU = 3 V inside the negative electrode was 1.37 ions/nm^2 for the slit geometry and 1.58 ions/nm^2 for the rough pore. Therefore, at ΔU = 3 V the additional enhancement of capacitance in rough pores comes from the increased density of counterions inside nanopores.

Single Chain Structural Elements. Next we examine the nanopores comprised of 1D-chains. The presence of short segments of single C-chains was suggested in TiC−CDC and B_4C−CDC electrodes.[105] Furthermore, such structural motifs also might be found in conductive polymers or porous carbides containing heteroatoms.[100,106−109] From the point of view of the electrochemical stability, the 1D-chains are expected to be less stable than the strongly bonded 2D networks. On the other hand, nanopores containing 1D-chains have the advantage of increased exposed SSA and therefore this electrode configuration can reveal the possible upper limits of non-Faradaic energy densities. For our purposes such electrode geometry models nanopores

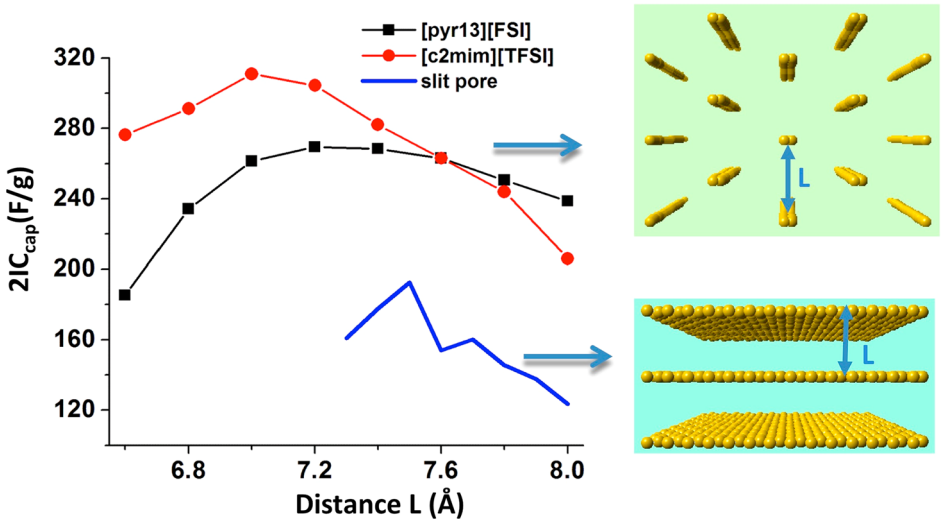

Figure 9. Dependence of $2IC_{cap}$ (in units of F/g electrode) on the nanopore widths for electrodes comprised of an array of 1D chains. Also shown is the estimated dependence of [C_2mim][TFSI] electrolyte inside an array of single graphene sheets.

with structural elements that have extreme atomic scale roughness and curvature. Previous works showed that cylinders with radius larger than 3 Å generate only a modest increase in capacitance,[110] however, decreasing the radius of cylinder to the limiting case of 1D-chains significantly increases the non-Faradaic capacitances.[111] The utilized simulation setup is illustrated in the snapshots of Figure 9. The geometry of positive and negative pores were the same. The distance L between chains, which is an effective measure of pore width, varied from 6.6 to 8.0 Å. The pores were considered as conductors, which is a reasonable approximation for realistic systems that have their electronic conductivity significantly increased by doping with heavy elements.[112,113]

Shown in Figure 9 is the $2IC_{cap}$ as a function of pore width (L) for [C_2mim][TFSI] and [pyr_{13}][FSI] electrolytes and potential difference of 3 V between electrodes. For these pores, we observe a relatively broad maximum in capacitance *versus* pore width. The capacities generated by single wires are ≈240−250F/g.[111] Therefore, the extra-enhancement due to nanoconfinement relative to the corresponding infinitely wide pore is rather modest for these geometries, *i.e.*, 10−15%. Smaller relative capacitance enhancements for this geometry (as compared to slits) could be explained by the lower density of conductive material (pore walls) that screens out the repulsion between counterions inside the pore. Indeed, the volumetric density of the pore atoms in Figure 9 was varied between 22 to 17 C atoms/nm^3 (or 0.43 to 0.34 g C/cm^3). For comparisons, the CDCs prepared by Largeot[56] were twice as dense (40 to 43 atom C/nm^3), and the theoretical exfoliated graphene with sheets separated by 7.5 Å (as in the pores studied in previous sections) has a density of conductive C of ∼50 atom C/nm^3 (or 1 g/cm^3). In spite of such sparser distribution of conducting electrode atoms, in the electrodes comprised of 1D-chain arrays there is still sufficient screening to keep the density of counterions inside the pores sufficiently elevated at 3 V and resulting in large non-Faradaic capacities of up to 300−310 F/g. For comparison in Figure 9 we also show an estimated capacitance (per mass of electrode material) that can be expected from exfoliated graphite where each graphene sheet has both of its sides exposed to electrolyte.

CONCLUSIONS

In order to understand the microscopic origin of the capacitance enhancement for the entire capacitor comprised of nanoporous electrodes and RTIL electrolytes, one have to consider two contributions: (i) the intrinsic capacitance of the corresponding "open structure" (*i.e.*, an infinitely wide pore) due to topography/structure of nanopore walls and (ii) the additional enhancement (relative to the infinitely wide pore) due to the nanoconfinement effect. The open structure for the slit and nanotube pores is a flat surface, and recent experiments[114,115] and chemically realistic simulations[116−118] showed that RTIL based electrolytes on atomically flat surfaces generate capacitance between 4 and 6 μF/cm^2. The simulations presented here show that the enhancement of the capacitance due to nanoconfinement in the subnanometer wide slits and cylinders accounts for ∼30−50% increase in capacitance relative to the corresponding open structure and, hence, these pores are only capable to enhance the capacitance up to ∼6−8 μF/cm^2. Nanopores with atomically rough walls generate larger capacitances, up to 11−12 μF/cm^2, which is comparable to the values observed in experiments. However, a significant part of this enhancement comes from the intrinsically higher values of the capacitance of atomically rough surfaces in the open structure and not due to nanoconfinement.

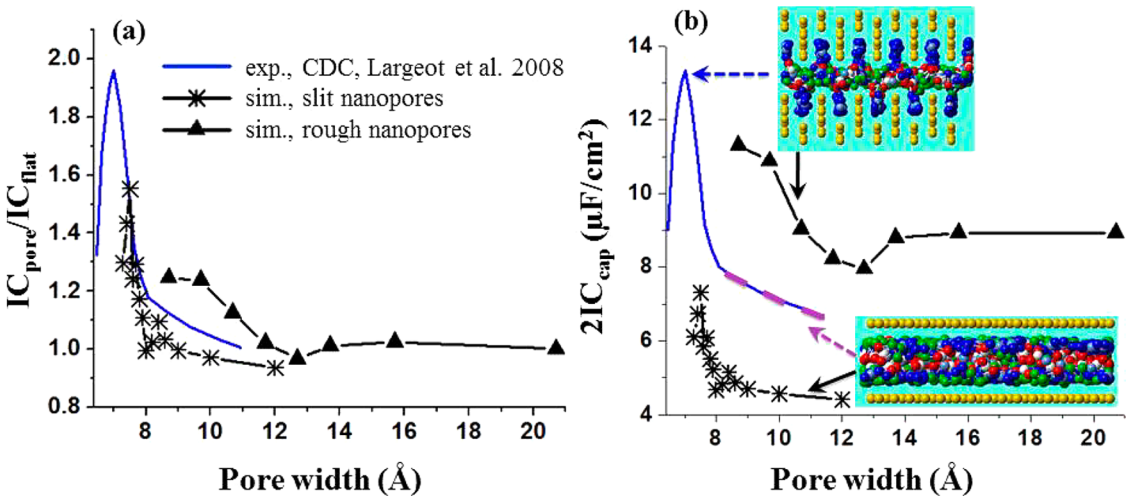

Figure 10. Comparison of integral capacitances obtained from simulations in atomically flat and rough slit pores as a function of pore dimensions for [C_2mim][TFSI] RTIL: (a) the total capacitance in nanopores normalized by the value obtained on the open structure flat electrode, (b) the absolute values of capacitances. Also shown are experimental data from ref 56 obtained for the same RTIL using CDC nanoporous electrodes.

The capacitance enhancement in the rough pores relative to their corresponding open structure is actually smaller (~25%) than the relative enhancement generated in slit pores. This is illustrated in Figure 10a where the capacitances for two types of pores are compared as a function of pore width.

Therefore, the experimentally reported capacitance enhancement up to ~13 μF/cm^2 (*i.e.*, ~100% increase compared to basal plane graphite) is likely not solely due to nanoconfinement by smooth surfaces. For real carbon based nanoporous structures, such as CDC nanopores, it is possible that the extent of surface roughness inside the pores depends on the nanopore width *i.e.*, the topography of the walls in the wider pores might be geometrically different than in the tighter ones. Indeed, examining snapshots of realistic CDCs structures[119−121] computed with the reverse Monte Carlo technique,[122] it appears that the walls of wider nanopores are smoother, made mostly of slightly curved graphene-like planes, and have a rather low concentration of rough edges exposed to electrolyte. In contrast, the tighter (subnanometer) CDC nanopores clearly have a higher density of edges inside them. On the basis of this observation and our conclusions discussed above, we propose that the capacitance enhancement shown, *e.g.*, in ref 56 is likely originated from the combined result of two effects: (i) the nanoconfinement and (ii) the change in the surface structure of the nanopore walls upon changing the nanopore dimensions. The first effect leads to an enhanced screening of ionic interactions due to the polarization of the electrode walls as proposed by Kondrat and Kornyshev. However, we believe that the second effect is equally important to the observed experimental enhancement. In the wider pores (>1 nm), the walls of CDC nanopores are relatively smooth and hence the charge storage and the

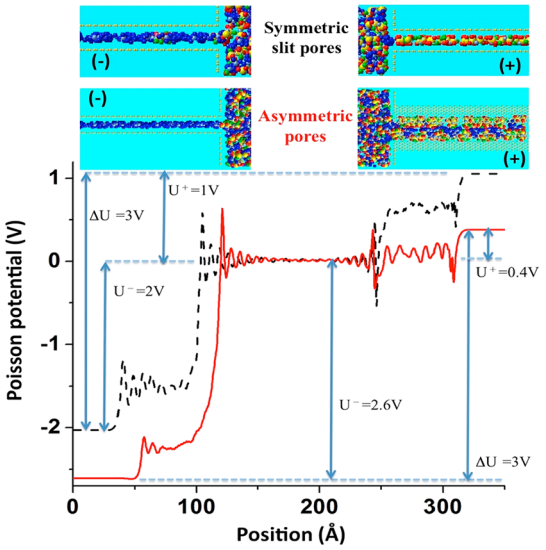

Figure 11. Poisson potential across simulation cell for systems containing [C_8mim][TFSI] electrolyte inside symmetric electrodes with slit atomically flat nanopores (black dash line) and asymmetric electrodes with the slit geometry for the negative electrode and atomically rough walls for the positive electrode (solid red line). Also shown the split of the total potential difference $\Delta U = 3$ V into potential drop between each electrode and bulk electrolyte outside of nanopores.

capacitance are similar to those observed in the MD simulations using atomically smooth slit pores. For CDC electrodes with narrower nanopores (<1 nm) we believe that the structure of the nanopore walls becomes significantly rougher and that the second effect contributes to the capacitance enhancement; *i.e.*, the CDC nanopores behave more like the atomically rough nanopores simulated here and shown in Figure 10b. For the nanopore structures and RTILs studied here, we quantify that the increase in the surface roughness contributes about 50% of the capacitance enhancement (or on average ~3 μF/cm^2) observed on CDC electrodes.

The results of this work indicate that the nanopore dimension is not the only key structural design parameter that can be varied to optimize the energy storage of EDL capacitors. The nanopore surface roughness and the mismatch in the chemical structure, the size, and the shape of the electrolyte cations and anions can also be used for such optimization. All these parameters can be tuned to increase the IC on individual electrodes as well as to minimize the asymmetry in $IC_{\pm}$ contributions to the total capacitance IC_{cap}. The asymmetric response of RTILs on the negative and positive nanporous electrodes also brings another practical concern: the electrochemical stability of the electrolyte. Figure 11 shows the Poisson potential across the simulation cell as obtained from simulations of $[C_8mim][TFSI]$ electrolyte at a potential difference of $\Delta U = 3$ V. Even in the case of symmetric electrodes the potential drop between the bulk electrolyte and the electrode surfaces depends on the electrode polarity. On the negative electrode, the electrolyte experiences a 2 V potential drop, while on the positive electrode only 1 V. The difference becomes even more pronounced if an asymmetric electrode set up is used. In the particular example shown in Figure 11 the nanopores on the positive and negative electrodes have equal volumes, but the surface roughness is quite different. This leads to an almost 2.6 V potential drop on the negative electrode and only 0.4 V on the positive one. These large differences in the electrode potential due to the asymmetric structure of ions and/or nanopores may promote the electrochemical decomposition of the electrolyte near the electrode with a larger potential drop at applied potentials ΔU that are lower than the nominal potential at which the electrolyte is considered to be electrochemically stable on the flat electrodes with the symmetric potential drops on the positive and negative electrodes.

METHODS

Simulation Protocol. The electrolytes were modeled using a combined united-atoms/all-atoms nonpolarizable forcefields presented and validated in our previous works for $[C_nmim][TFSI]$,[123] for $[pyr_{13}][FSI]$,[124] for $[C_4mim][PF_6]$,[116] and for $[C_nmim][FSI]$.[95] Each system contained between 300 and 500 ionic pairs (depending on the system and the pore geometry) which is sufficient to create a substantial amount of bulk electrolyte separating two electrodes and hence to ensure that the EDL structures formed on one electrode do not influence the EDLs on the other electrode. The simulations were performed using a methodology that allows imposing a constant potential difference between electrodes. The nanopore walls were modeled as a conductor[125,126] and treating the electrode atoms as polarizable with their polarizabilities represented by Gaussian distributed charges with a width of 0.5 Å.[125,127] Reed *et al.*[125] and Sprick *et al.*[128] showed that the width of 0.5 Å for Gaussian charge distribution reproduces the well-known phenomenological results for planar capacitors made of parallel conductive plates. Also, it was shown that the electrostatic energy is almost independent of small variations in the widths of Gaussian charge distribution.[129] The electrode charges were computed on-the-fly by optimizing the total electrostatic energy *via* self-consistent iterations. Note that the condition of minimizing the electrostatic energy in this setup is equivalent to imposing a certain potential on the electrode atoms and finding the set of electrode surface charges that satisfy this constrain. The electrostatic forces were computed utilizing smooth particle mesh Ewald adapted for the 2D geometry.[130−133] Additional details regarding this simulation method can be found in refs 134−138.

A time-reversible multiple time-step algorithm[139] was utilized to integrate the equations of motion with the following time steps: a 0.5 fs step for forces from bonds and bends, a 2.5 fs step for forces due to dihedrals and nonbonded interactions within 7.5 Å cut off, and a 5 fs step for the remaining long-range nonbonded interactions and the reciprocal part of electrostatic interactions. The charge distributions on the electrode surfaces were updated every 250 fs (*i.e.*, the electrostatic energy minimization step with constant applied potential difference constrain). The temperature was controlled with Nose−Hoover[140] chain thermostat applied to each molecule independently.[141] The systems were prepared as follows: an equilibrated bulk electrolyte was exposed to empty electrodes with desired applied potential difference between the electrodes but empty nanopores. The entrance to nanopores was blocked by a repulsive gate wall. Then the electrolyte was allowed to slowly enter the nanopore by moving the gate at a rate of 1.5−2.0 Å/ns. The slow insertion of the electrolyte into the charged pores helped to establish an equilibrium composition of ions inside the nanopore and prevent artificial trapping of co-ions. After the electrolyte insertion, all systems were equilibrated for several nanoseconds followed by production runs over 12−25 ns.

Analysis. The trajectories generated from simulations were used to calculate the density, spatial charge, and Poisson potential profiles across the simulation cells. The Poisson potential $\varphi(z)$ was obtained by integrating the Poisson equation for the spatial charge density. The potential drop in EDL, U_{EDL}, was defined as the difference between the Poisson potential on the electrode surface and in bulk electrolyte, $U_{EDL} = \varphi_{electrode} - \varphi_{bulk}$. The potential drop within EDL at uncharged surfaces defines the potential of zero charge (PZC) and the electrode potential, $U_{\pm}$, on individual electrodes was defined as the difference between EDL potential drop and PZC, $U_{\pm} = U_{EDL} - PZC$. The dependencies of the electrode charge surface density (σ) *vs* potential $U_{electrode}$ obtained from simulations were used to calculate (i) the differential capacity, DC, as the derivative of electrode charge *versus* electrode potential, $DC = d\sigma/dU_{\pm}$, (ii) the integral capacitance of individual electrodes, $IC_{\pm} = \sigma/U_{\pm}$, and (iii) the integral capacitance of the entire capacitor $IC_{cap} = \sigma/\Delta U$, where ΔU is the dialed potential difference between electrodes/pores. We estimate that the error bars for obtained DC are not exceeding 10% while uncertainties for IC are even smaller because it does not involve numerical approximation of charge derivatives. The details of numerical procedures for the calculation of DC and IC as well as the estimates of the error bars can be found in our previous manuscripts.[92,117]

Note that the IC_{cap} is about factor of 2 smaller than the capacity of individual electrodes. To facilitate the comparison we show twice the IC_{cap}, $2IC_{cap} = \sigma/(\Delta U/2)$, which has a similar magnitude as the electrode capacitance. Also, the experimental works are often reporting the specific capacitance defined as $2IC_{cap}$, see *e.g.*, ref 56, and therefore it allows a straightforward comparison of our simulation data with experiments. Analysis of the total capacitance rather than the contributions from individual electrodes has several advantages. First, the total capacitance reflects the actual charge stored by the capacitor. While individual electrodes can show quite different (asymmetric) capacitance dependencies (due to, *e.g.*, the defined potential scale), it is more important if their combined effect results in a capacitance increase. Second, the exact IC^+ and IC^- values depend on the value of PZC and on the accuracy of the integration of the Poisson potential, yet the computation of

the total capacitance does not require determination of PZC but only the potential difference between the two electrodes.

Finally, for the considered atomically rough surfaces the SSA was estimated by counting how many surface atoms are exposed to electrolyte. For the considered here topography the estimated SSA was 1.85 times the cross-sectional area of the system. In other words, the capacitances shown for rough surfaces already take into account the intrinsic increase of the accessible surface area with increasing surface roughness.

Conflict of Interest: The authors declare no competing financial interest.

Acknowledgment. The financial support of US Department of Energy through the SISGR Program Grant Number DECS00001912 is gratefully acknowledged. J.V. also acknowledges the National Science Foundation MRSEC (Grant # DMR 11-21252) for the partial support of his efforts to enhance molecular simulation methodology used in this work.

REFERENCES AND NOTES

1. Rebelo, L. P. N.; Canongia Lopes, J. N.; Esperança, J. M. S. S.; Filipe, E. On the Critical Temperature, Normal Boiling Point, and Vapor Pressure of Ionic Liquids. *J. Phys. Chem. B* **2005**, *109*, 6040–6043.
2. Paduszyński, K.; Domańska, U. Thermodynamic Modeling of Ionic Liquid Systems: Development and Detailed Overview of Novel Methodology Based on the Pc-Saft. *J. Phys. Chem. B* **2012**, *116*, 5002–5018.
3. Fox, D. M.; Awad, W. H.; Gilman, J. W.; Maupin, P. H.; De Long, H. C.; Trulove, P. C. Flammability, Thermal Stability, and Phase Change Characteristics of Several Trialkylimidazolium Salts. *Green Chem.* **2003**, *5*, 724–727.
4. Rosol, Z. P.; German, N. J.; Gross, S. M. Solubility, Ionic Conductivity and Viscosity of Lithium Salts in Room Temperature Ionic Liquids. *Green Chem.* **2009**, *11*, 1453–1457.
5. Tshibangu, P. N.; Ndwandwe, S. N.; Dikio, E. D. Density, Viscosity and Conductivity Study of 1-Butyl-3-Methylimidazolium Bromide. *Int. J. Electrochem. Sci.* **2011**, *6*, 2201–2213.
6. Cui, W.-W.; Tang, D.-Y.; Gong, Z.-L. Electrospun Poly-(Vinylidene Fluoride)/Poly(Methyl Methacrylate) Grafted TiO_2 Composite Nanofibrous Membrane as Polymer Electrolyte for Lithium-Ion Batteries. *J. Power Sources* **2013**, *223*, 206–213.
7. Dam, D. T.; Wang, X.; Lee, J.-M. Fabrication of a Mesoporous $Co(OH)_2$/Ito Nanowire Composite Electrode and Its Application in Supercapacitors. *RSC Adv.* **2012**, *2*, 10512–10518.
8. Patil, D. S.; Pawar, S. A.; Devan, R. S.; Gang, M. G.; Ma, Y.-R.; Kim, J. H.; Patil, P. S. Electrochemical Supercapacitor Electrode Material Based on Polyacrylic Acid/Polypyrrole/Silver Composite. *Electrochim. Acta* **2013**, *105*, 569–577.
9. Patil, D. S.; Shaikh, J. S.; Pawar, S. A.; Devan, R. S.; Ma, Y. R.; Moholkar, A. V.; Kim, J. H.; Kalubarme, R. S.; Park, C. J.; Patil, P. S. Investigations on Silver/Polyaniline Electrodes for Electrochemical Supercapacitors. *Phys. Chem. Chem. Phys.* **2012**, *14*, 11886–11895.
10. Shaikh, J.; Pawar, R.; Mali, S.; Moholkar, A.; Kim, J. H.; Patil, P. Effect of Annealing on the Supercapacitor Performance of Cuo-Paa/Cnt Films. *J. Solid State Electrochem.* **2012**, *16*, 25–33.
11. Ismail, Y. A.; Chang, J.; Shin, S. R.; Mane, R. S.; Han, S. H.; Kim, S. J. Hydrogel-Assisted Polyaniline Microfiber as Controllable Electrochemical Actuatable Supercapacitor. *J. Electrochem. Soc.* **2009**, *156*, A313–A317.
12. Rao, V. G.; Banerjee, C.; Ghosh, S.; Mandal, S.; Kuchlyan, J.; Sarkar, N. A Step toward the Development of High-Temperature Stable Ionic Liquid-in-Oil Microemulsions Containing Double-Chain Anionic Surface Active Ionic Liquid. *J. Phys. Chem. B* **2013**, *117*, 7472–7480.
13. Li, D.; Pang, Z.; Wang, Q.; Ke, H.; Cai, Y.; Xu, Y.; Huang, F.; Wei, Q. Fabrication and Characterization of Polyamide6-Room Temperature Ionic Liquid (Pa6-RTIL) Composite Nanofibers by Electrospinning. *Fibers Polym.* **2013**, *14*, 1614–1619.
14. Hueso, K. B.; Armand, M.; Rojo, T. High Temperature Sodium Batteries: Status, Challenges and Future Trends. *Energy Environ. Sci.* **2013**, *6*, 734–749.
15. Zhong, H.; Xu, F.; Li, Z.; Fu, R.; Wu, D. High-Energy Supercapacitors Based on Hierarchical Porous Carbon with an Ultrahigh Ion-Accessible Surface Area in Ionic Liquid Electrolytes. *Nanoscale* **2013**, *5*, 4678–4682.
16. Shen, W.; Hu, T.; Wang, P.; Sun, H.; Fan, W. Hollow Porous Carbon Fiber from Cotton with Nitrogen Doping. *ChemPlusChem* **2014**, *79*, 284–289.
17. Li, Y.; Li, Z.; Shen, P. K. Simultaneous Formation of Ultrahigh Surface Area and Three-Dimensional Hierarchical Porous Graphene-Like Networks for Fast and Highly Stable Supercapacitors. *Adv. Mater.* **2013**, *25*, 2474–2480.
18. Fedorov, M. V.; Kornyshev, A. A. Ionic Liquids at Electrified Interfaces. *Chem. Rev.* **2014**, *114*, 2978–3036.
19. Yu, A.; Chabot, V.; Zhang, J. *Electrochemical Supercapacitors for Energy Storage and Delivery: Fundamentals and Applications*; CRC Press: Boca Raton, FL, 2013.
20. Cote, L. J.; Cruz-Silva, R.; Huang, J. Flash Reduction and Patterning of Graphite Oxide and Its Polymer Composite. *J. Am. Chem. Soc.* **2009**, *131*, 11027–11032.
21. Wang, W.; Guo, S.; Lee, I.; Ahmed, K.; Zhong, J.; Favors, Z.; Zaera, F.; Ozkan, M.; Ozkan, C. S. Hydrous Ruthenium Oxide Nanoparticles Anchored to Graphene and Carbon Nanotube Hybrid Foam for Supercapacitors. *Sci. Rep.* **2014**, *4*, 4452.
22. Kornyshev, A. A. Double-Layer in Ionic Liquids: Paradigm Change? *J. Phys. Chem. B* **2007**, *111*, 5545–5557.
23. Oldham, K. B. A Gouy–Chapman–Stern Model of the Double Layer at a (Metal)/(Ionic Liquid) Interface. *J. Electroanal. Chem.* **2008**, *613*, 131–138.
24. Forsman, J.; Woodward, C. E.; Trulsson, M. A Classical Density Functional Theory of Ionic Liquids. *J. Phys. Chem. B* **2011**, *115*, 4606–4612.
25. Sarkisov, L.; Van Tassel, P. R. Theories of Molecular Fluids Confined in Disordered Porous Materials. *J. Phys.: Condens. Matter* **2008**, *20*, 333101.
26. Lu, W.; Chung, D. D. L. Preparation of Conductive Carbons with High Surface Area. *Carbon* **2001**, *39*, 39–44.
27. Laurent, C.; Peigney, A.; Dumortier, O.; Rousset, A. Carbon Nanotubes–Fe–Alumina Nanocomposites. Part II: Microstructure and Mechanical Properties of the Hot-Pressed Composites. *J. Eur. Ceram. Soc.* **1998**, *18*, 2005–2013.
28. Inoue, S.; Ichikuni, N.; Suzuki, T.; Uematsu, T.; Kaneko, K. Capillary Condensation of N_2 on Multiwall Carbon Nanotubes. *J. Phys. Chem. B* **1998**, *102*, 4689–4692.
29. Pinkert, K.; Oschatz, M.; Borchardt, L.; Klose, M.; Zier, M.; Nickel, W.; Giebeler, L.; Oswald, S.; Kaskel, S.; Eckert, J. Role of Surface Functional Groups in Ordered Mesoporous Carbide-Derived Carbon/Ionic Liquid Electrolyte Double-Layer Capacitor Interfaces. *ACS Appl. Mater. Interfaces* **2014**, *6*, 2922–2928.
30. Chakrabarti, M. H.; Brandon, N. P.; Hajimolana, S. A.; Tariq, F.; Yufit, V.; Hashim, M. A.; Hussain, M. A.; Low, C. T. J.; Aravind, P. V. Application of Carbon Materials in Redox Flow Batteries. *J. Power Sources* **2014**, *253*, 150–166.
31. Cui, C.; Qian, W.; Yu, Y.; Kong, C.; Yu, B.; Xiang, L.; Wei, F. Highly Electroconductive Mesoporous Graphene Nanofibers and Their Capacitance Performance at 4 V. *J. Am. Chem. Soc.* **2014**, *136*, 2256–2259.
32. Chmiola, J.; Yushin, G.; Gogotsi, Y.; Portet, C.; Simon, P.; Taberna, P. L. Anomalous Increase in Carbon Capacitance at Pore Sizes Less Than 1 Nanometer. *Science* **2006**, *313*, 1760–1763.
33. Simon, P.; Gogotsi, Y. Materials for Electrochemical Capacitors. *Nat. Mater.* **2008**, *7*, 845–854.
34. Lin, R.; Taberna, P. L.; Chmiola, J.; Guay, D.; Gogotsi, Y.; Simon, P. Microelectrode Study of Pore Size, Ion Size, and Solvent Effects on the Charge/Discharge Behavior of Microporous Carbons for Electrical Double-Layer Capacitors. *J. Electrochem. Soc.* **2009**, *156*, A7–A12.
35. Wu, C.; Deng, S.; Wang, H.; Sun, Y.; Liu, J.; Yan, H. Preparation of Novel Three-Dimensional Nio/Ultrathin

Derived Graphene Hybrid for Supercapacitor Applications. *ACS Appl. Mater. Interfaces* **2014**, *6*, 1106–1112.
36. Calvo, E. G.; Lufrano, F.; Staiti, P.; Brigandì, A.; Arenillas, A.; Menéndez, J. A. Optimizing the Electrochemical Performance of Aqueous Symmetric Supercapacitors Based on an Activated Carbon Xerogel. *J. Power Sources* **2013**, *241*, 776–782.
37. Ji, C. C.; Xu, M. W.; Bao, S. J.; Lu, Z. J.; Cai, C. J.; Chai, H.; Wang, R. Y.; Yang, F.; Wei, H. Self-Assembled Three-Dimensional Interpenetrating Porous Graphene Aerogels with MnO_2 Coating and Their Application as High-Performance Supercapacitors. *New J. Chem.* **2013**, *37*, 4199–4205.
38. Peng, Q.; Li, Y.; He, X.; Gui, X.; Shang, Y.; Wang, C.; Wang, C.; Zhao, W.; Du, S.; Shi, E.; *et al.* Graphene Nanoribbon Aerogels Unzipped from Carbon Nanotube Sponges. *Adv. Mater.* **2014**, *26*, 3241–3247.
39. Li, P.; Kong, C.; Shang, Y.; Shi, E.; Yu, Y.; Qian, W.; Wei, F.; Wei, J.; Wang, K.; Zhu, H.; *et al.* Highly Deformation-Tolerant Carbon Nanotube Sponges as Supercapacitor Electrodes. *Nanoscale* **2013**, *5*, 8472–8479.
40. Niu, C.; Sichel, E. K.; Hoch, R.; Moy, D.; Tennent, H. High Power Electrochemical Capacitors Based on Carbon Nanotube Electrodes. *Appl. Phys. Lett.* **1997**, *70*, 1480–1482.
41. Jiang, H.; Li, C.; Sun, T.; Ma, J. A Green and High Energy Density Asymmetric Supercapacitor Based on Ultrathin MnO_2 Nanostructures and Functional Mesoporous Carbon Nanotube Electrodes. *Nanoscale* **2012**, *4*, 807–812.
42. Lin, C.; Ritter, J. A.; Popov, B. N. Characterization of Sol-Gel-Derived Cobalt Oxide Xerogels as Electrochemical Capacitors. *J. Electrochem. Soc.* **1998**, *145*, 4097–4103.
43. Curran, S. A.; Ajayan, P. M.; Blau, W. J.; Carroll, D. L.; Coleman, J. N.; Dalton, A. B.; Davey, A. P.; Drury, A.; McCarthy, B.; Maier, S.; *et al.* A Composite from Poly(M-Phenylenevinylene-Co-2,5-Dioctoxy-P-Phenylenevinylene) and Carbon Nanotubes: A Novel Material for Molecular Optoelectronics. *Adv. Mater.* **1998**, *10*, 1091–1093.
44. Markoulidis, F.; Lei, C.; Lekakou, C.; Duff, D.; Khalil, S.; Martorana, B.; Cannavaro, I. A Method to Increase the Energy Density of Supercapacitor Cells by the Addition of Multiwall Carbon Nanotubes into Activated Carbon Electrodes. *Carbon* **2014**, *68*, 58–66.
45. Chen, H.; Wang, H.; Yang, L.; Xiao, Y.; Zheng, M.; Liu, Y.; Fu, H. High Specific Surface Area Rice Hull Based Porous Carbon Prepared for EDLCs. *Int. J. Electrochem. Sci.* **2012**, *7*, 4889–4897.
46. Zhang, L.; Zhang, F.; Yang, X.; Long, G.; Wu, Y.; Zhang, T.; Leng, K.; Huang, Y.; Ma, Y.; Yu, A. Porous 3d Graphene-Based Bulk Materials with Exceptional High Surface Area and Excellent Conductivity for Supercapacitors. *Sci. Rep.* **2013**, *3*, 1408.
47. Farha, O. K.; Eryazici, I.; Jeong, N. C.; Hauser, B. G.; Wilmer, C. E.; Sarjeant, A. A.; Snurr, R. Q.; Nguyen, S. T.; Yazaydın, A. Ö.; Hupp, J. T. Metal−Organic Framework Materials with Ultrahigh Surface Areas: Is the Sky the Limit? *J. Am. Chem. Soc.* **2012**, *134*, 15016–15021.
48. Sarkisov, L. Accessible Surface Area of Porous Materials: Understanding Theoretical Limits. *Adv. Mater.* **2012**, *24*, 3130–3133.
49. Barbieri, O.; Hahn, M.; Herzog, A.; Kötz, R. Capacitance Limits of High Surface Area Activated Carbons for Double Layer Capacitors. *Carbon* **2005**, *43*, 1303–1310.
50. Ji, H.; Zhao, X.; Qiao, Z.; Jung, J.; Zhu, Y.; Lu, Y.; Zhang, L. L.; MacDonald, A. H.; Ruoff, R. S. Capacitance of Carbon-Based Electrical Double-Layer Capacitors. *Nat. Commun.* **2014**, *5*, 3317.
51. Doh, C.-H.; Kim, H.-S.; Moon, S.-I. A Study on the Irreversible Capacity of Initial Doping/Undoping of Lithium into Carbon. *J. Power Sources* **2001**, *101*, 96–102.
52. Vix-Guterl, C.; Frackowiak, E.; Jurewicz, K.; Friebe, M.; Parmentier, J.; Béguin, F. Electrochemical Energy Storage in Ordered Porous Carbon Materials. *Carbon* **2005**, *43*, 1293–1302.
53. Jänes, A.; Permann, L.; Arulepp, M.; Lust, E. Electrochemical Characteristics of Nanoporous Carbide-Derived Carbon Materials in Non-Aqueous Electrolyte Solutions. *Electrochem. Commun.* **2004**, *6*, 313–318.
54. Balducci, A.; Dugas, R.; Taberna, P. L.; Simon, P.; Plée, D.; Mastragostino, M.; Passerini, S. High Temperature Carbon−Carbon Supercapacitor Using Ionic Liquid as Electrolyte. *J. Power Sources* **2007**, *165*, 922–927.
55. Kondrat, S.; Wu, P.; Qiao, R.; Kornyshev, A. A. Accelerating Charging Dynamics in Subnanometre Pores. *Nat. Mater.* **2014**, *13*, 387–393.
56. Largeot, C.; Portet, C.; Chmiola, J.; Taberna, P.-L.; Gogotsi, Y.; Simon, P. Relation between the Ion Size and Pore Size for an Electric Double-Layer Capacitor. *J. Am. Chem. Soc.* **2008**, *130*, 2730–2731.
57. Fernández, J. A.; Arulepp, M.; Leis, J.; Stoeckli, F.; Centeno, T. A. Edlc Performance of Carbide-Derived Carbons in Aprotic and Acidic Electrolytes. *Electrochim. Acta* **2008**, *53*, 7111–7116.
58. Centeno, T. A.; Sereda, O.; Stoeckli, F. Capacitance in Carbon Pores of 0.7 to 15 Nm: A Regular Pattern. *Phys. Chem. Chem. Phys.* **2011**, *13*, 12403–12406.
59. Lota, G.; Centeno, T. A.; Frackowiak, E.; Stoeckli, F. Improvement of the Structural and Chemical Properties of a Commercial Activated Carbon for Its Application in Electrochemical Capacitors. *Electrochim. Acta* **2008**, *53*, 2210–2216.
60. Centeno, T. A.; Hahn, M.; Fernández, J. A.; Kötz, R.; Stoeckli, F. Correlation between Capacitances of Porous Carbons in Acidic and Aprotic Edlc Electrolytes. *Electrochem. Commun.* **2007**, *9*, 1242–1246.
61. Feng, G.; Cummings, P. T. Supercapacitor Capacitance Exhibits Oscillatory Behavior as a Function of Nanopore Size. *J. Phys. Chem. Lett.* **2011**, *2*, 2859–2864.
62. Ohba, T.; Kaneko, K. Competition of Desolvation and Stabilization of Organic Electrolytes in Extremely Narrow Nanopores. *J. Phys. Chem. C* **2013**, *117*, 17092–17098.
63. Shim, Y.; Jung, Y.; Kim, H. J. Graphene-Based Supercapacitors: A Computer Simulation Study. *J. Phys. Chem. C* **2011**, *115*, 23574–23583.
64. Wu, P.; Huang, J.; Meunier, V.; Sumpter, B. G.; Qiao, R. Complex Capacitance Scaling in Ionic Liquids-Filled Nanopores. *ACS Nano* **2011**, *5*, 9044–9051.
65. Wu, P.; Huang, J.; Meunier, V.; Sumpter, B. G.; Qiao, R. Voltage Dependent Charge Storage Modes and Capacity in Subnanometer Pores. *J. Phys. Chem. Lett.* **2012**, *3*, 1732–1737.
66. Merlet, C.; Rotenberg, B.; Madden, P. A.; Taberna, P.-L.; Simon, P.; Gogotsi, Y.; Salanne, M. On the Molecular Origin of Supercapacitance in Nanoporous Carbon Electrodes. *Nat. Mater.* **2012**, *11*, 306–310.
67. Kondrat, S.; Perez, C. R.; Presser, V.; Gogotsi, Y.; Kornyshev, A. A. Effect of Pore Size and Its Dispersity on the Energy Storage in Nanoporous Supercapacitors. *Energy Environ. Sci.* **2012**, *5*, 6474–6479.
68. Merlet, C.; Forse, A. C.; Griffin, J. M.; Frenkel, D.; Grey, C. P. Lattice Simulation Method to Model Diffusion and NMR Spectra in Porous Materials. *J. Chem. Phys.* **2015**, *142*, 094701.
69. Merlet, C.; Péan, C.; Rotenberg, B.; Madden, P. A.; Daffos, B.; Taberna, P. L.; Simon, P.; Salanne, M. Highly Confined Ions Store Charge More Efficiently in Supercapacitors. *Nat. Commun.* **2013**, *4*, 2701.
70. Skinner, B.; Chen, T.; Loth, M. S.; Shklovskii, B. I. Theory of Volumetric Capacitance of an Electric Double-Layer Supercapacitor. *Phys. Rev. E: Stat., Nonlinear, Soft Matter Phys.* **2011**, *83*, 056102.
71. Loth, M. S.; Skinner, B.; Shklovskii, B. I. Anomalously Large Capacitance of an Ionic Liquid Described by the Restricted Primitive Model. *Phys. Rev. E: Stat., Nonlinear, Soft Matter Phys.* **2010**, *82*, 056102.
72. Henderson, D. Oscillations in the Capacitance of a Nanopore Containing an Electrolyte Due to Pore Width and Nonzero Size Ions. *J. Colloid Interface Sci.* **2012**, *374*, 345–347.

73. Pizio, O.; Sokołowski, S. Restricted Primitive Model for Electrolyte Solutions in Slit-Like Pores with Grafted Chains: Microscopic Structure, Thermodynamics of Adsorption, and Electric Properties from a Density Functional Approach. *J. Chem. Phys.* **2013**, *138*, 204715.
74. Jiang, D.-e.; Jin, Z.; Wu, J. Oscillation of Capacitance inside Nanopores. *Nano Lett.* **2011**, *11*, 5373–5377.
75. Lee, A. A.; Kondrat, S.; Kornyshev, A. A. Single-File Charge Storage in Conducting Nanopores. *Phys. Rev. Lett.* **2014**, *113*, 048701.
76. Jiang, D.-e.; Wu, J. Unusual Effects of Solvent Polarity on Capacitance for Organic Electrolytes in a Nanoporous Electrode. *Nanoscale* **2014**, *6*, 5545–5550.
77. Jiang, D.-e.; Jin, Z.; Henderson, D.; Wu, J. Solvent Effect on the Pore-Size Dependence of an Organic Electrolyte Supercapacitor. *J. Phys. Chem. Lett.* **2012**, *3*, 1727–1731.
78. Huang, J.; Sumpter, B. G.; Meunier, V. A Universal Model for Nanoporous Carbon Supercapacitors Applicable to Diverse Pore Regimes, Carbon Materials, and Electrolytes. *Chem.—Eur. J.* **2008**, *14*, 6614–6626.
79. Outhwaite, C. W.; Lamperski, S.; Bhuiyan, L. B. Influence of Electrode Polarization on the Capacitance of an Electric Double Layer at and around Zero Surface Charge. *Mol. Phys.* **2010**, *109*, 21–26.
80. Huang, J.; Sumpter, B. G.; Meunier, V. Theoretical Model for Nanoporous Carbon Supercapacitors. *Angew. Chem., Int. Ed.* **2008**, *47*, 520–524.
81. Reszko-Zygmunt, J.; Sokołowski, S.; Henderson, D.; Boda, D. Temperature Dependence of the Double Layer Capacitance for the Restricted Primitive Model of an Electrolyte Solution from a Density Functional Approach. *J. Chem. Phys.* **2005**, *122*, 084504.
82. Lamperski, S.; Sosnowska, J.; Bhuiyan, L. B.; Henderson, D. Size Asymmetric Hard Spheres as a Convenient Model for the Capacitance of the Electrical Double Layer of an Ionic Liquid. *J. Chem. Phys.* **2014**, *140*, 014704.
83. Ivaništšev, V.; Fedorov, M. V.; Lynden-Bell, R. M. Screening of Ion−Graphene Electrode Interactions by Ionic Liquids: The Effects of Liquid Structure. *J. Phys. Chem. C* **2014**, *118*, 5841–5847.
84. Burt, R.; Birkett, G.; Zhao, X. S. A Review of Molecular Modelling of Electric Double Layer Capacitors. *Phys. Chem. Chem. Phys.* **2014**, *16*, 6519–6538.
85. Outhwaite, C. W.; Bhuiyan, L. B. The Point Ion Modified Poisson−Boltzmann Theory for a Planar Electric Double Layer with Different Permittivities for the Electrode, Inner Layer and Diffuse Layer. *Mol. Phys.* **2014**, *112*, 2963–2969.
86. Torrie, G. M.; Valleau, J. P.; Patey, G. N. Electrical Double Layers. II. Monte Carlo and HNC Studies of Image Effects. *J. Chem. Phys.* **1982**, *76*, 4615–4622.
87. Valiskó, M.; Boda, D. The Effect of Concentration- and Temperature-Dependent Dielectric Constant on the Activity Coefficient of NaCl Electrolyte Solutions. *J. Chem. Phys.* **2014**, *140*, 234508.
88. Boda, D.; Csányi, É.; Gillespie, D.; Kristóf, T. Dynamic Monte Carlo Simulation of Coupled Transport through a Narrow Multiply-Occupied Pore. *J. Phys. Chem. C* **2014**, *118*, 700–707.
89. Kondrat, S.; Kornyshev, A. Superionic State in Double-Layer Capacitors with Nanoporous Electrodes. *J. Phys.: Condens. Matter* **2011**, *23*, 022201.
90. Kondrat, S.; Georgi, N.; Fedorov, M. V.; Kornyshev, A. A. A Superionic State in Nano-Porous Double-Layer Capacitors: Insights from Monte Carlo Simulations. *Phys. Chem. Chem. Phys.* **2011**, *13*, 11359–11366.
91. Kornyshev, A. A. The Simplest Model of Charge Storage in Single File Metallic Nanopores. *Faraday Discuss.* **2013**, *164*, 117–133.
92. Xing, L.; Vatamanu, J.; Borodin, O.; Bedrov, D. On the Atomistic Nature of Capacitance Enhancement Generated by Ionic Liquid Electrolyte Confined in Subnanometer Pores. *J. Phys. Chem. Lett.* **2012**, *4*, 132–140.
93. Xu, J.; Gao, Q.; Zhang, Y.; Tan, Y.; Tian, W.; Zhu, L.; Jiang, L. Preparing Two-Dimensional Microporous Carbon from Pistachio Nutshell with High Areal Capacitance as Supercapacitor Materials. *Sci. Rep.* **2014**, *4*, 5545.
94. Rica, R. A.; Ziano, R.; Salerno, D.; Mantegazza, F.; Bazant, M. Z.; Brogioli, D. Electro-Diffusion of Ions in Porous Electrodes for Capacitive Extraction of Renewable Energy from Salinity Differences. *Electrochim. Acta* **2013**, *92*, 304–314.
95. Hu, Z.; Vatamanu, J.; Borodin, O.; Bedrov, D. A Comparative Study of Alkylimidazolium Room Temperature Ionic Liquids with FSI and TFSI Anions near Charged Electrodes. *Electrochim. Acta* **2014**, *145*, 40–52.
96. Kiyohara, K.; Shioyama, H.; Sugino, T.; Asaka, K. Phase Transition in Porous Electrodes. II. Effect of Asymmetry in the Ion Size. *J. Chem. Phys.* **2012**, *136*, 094701.
97. Kiyohara, K.; Sugino, T.; Asaka, K. Phase Transition in Porous Electrodes. *J. Chem. Phys.* **2011**, *134*, 154710.
98. Raabe, G.; Köhler, J. Thermodynamical and Structural Properties of Binary Mixtures of Imidazolium Chloride Ionic Liquids and Alcohols from Molecular Simulation. *J. Chem. Phys.* **2008**, *129*, 144503.
99. Henderson, D.; Lamperski, S.; Bari Bhuiyan, L.; Wu, J. The Tail Effect on the Shape of an Electrical Double Layer Differential Capacitance Curve. *J. Chem. Phys.* **2013**, *138*, 144704.
100. Aida, T.; Fukushima, T. Soft Materials with Graphitic Nanostructures. *Philos. Trans. R. Soc. London, Ser. A* **2007**, *365*, 1539–1552.
101. Vatamanu, J.; Cao, L.; Borodin, O.; Bedrov, D.; Smith, G. D. On the Influence of Surface Topography on the Electric Double Layer Structure and Differential Capacitance of Graphite/Ionic Liquid Interfaces. *J. Phys. Chem. Lett.* **2011**, *2*, 2267–2272.
102. Xing, L.; Vatamanu, J.; Smith, G. D.; Bedrov, D. Nanopatterning of Electrode Surfaces as a Potential Route to Improve the Energy Density of Electric Double-Layer Capacitors: Insight from Molecular Simulations. *J. Phys. Chem. Lett.* **2012**, *3*, 1124–1129.
103. Bedrov, D.; Vatamanu, J.; Hu, Z. Ionic Liquids at Charged Surfaces: Insight from Molecular Simulations. *J. Non-Cryst. Solids* **2015**, *407*, 339–348.
104. Ho, T. A.; Striolo, A. Capacitance Enhancement *via* Electrode Patterning. *J. Chem. Phys.* **2013**, *139*, 204708.
105. Kravchik, A. E.; Kukushkina, J. A.; Sokolov, V. V.; Tereshchenko, G. F. Structure of Nanoporous Carbon Produced from Boron Carbide. *Carbon* **2006**, *44*, 3263–3268.
106. Singh, V. V.; Nigam, A. K.; Batra, A.; Boopathi, M.; Singh, B.; Vijayaraghavan, R. Applications of Ionic Liquids in Electrochemical Sensors and Biosensors. *Int. J. Electrochem. Sci.* **2012**, *2012*, 165683.
107. Lu, W.; Fadeev, A. G.; Qi, B.; Smela, E.; Mattes, B. R.; Ding, J.; Spinks, G. M.; Mazurkiewicz, J.; Zhou, D.; Wallace, G. G.; *et al.* Use of Ionic Liquids for π-Conjugated Polymer Electrochemical Devices. *Science* **2002**, *297*, 983–987.
108. Reddy, K. M.; Liu, P.; Hirata, A.; Fujita, T.; Chen, M. W. Atomic Structure of Amorphous Shear Bands in Boron Carbide. *Nat. Commun.* **2013**, *4*, 2483.
109. Lin, H.; Li, L.; Ren, J.; Cai, Z.; Qiu, L.; Yang, Z.; Peng, H. Conducting Polymer Composite Film Incorporated with Aligned Carbon Nanotubes for Transparent, Flexible and Efficient Supercapacitor. *Sci. Rep.* **2013**, *3*, 1353.
110. Yang, L.; Fishbine, B. H.; Migliori, A.; Pratt, L. R. Molecular Simulation of Electric Double-Layer Capacitors Based on Carbon Nanotube Forests. *J. Am. Chem. Soc.* **2009**, *131*, 12373–12376.
111. Vatamanu, J.; Hu, Z.; Bedrov, D.; Perez, C.; Gogotsi, Y. Increasing Energy Storage in Electrochemical Capacitors with Ionic Liquid Electrolytes and Nanostructured Carbon Electrodes. *J. Phys. Chem. Lett.* **2013**, *4*, 2829–2837.
112. Heeger, A. J.; Kivelson, S.; Schrieffer, J. R.; Su, W. P. Solitons in Conducting Polymers. *Rev. Mod. Phys.* **1988**, *60*, 781–850.
113. Snook, G. A.; Kao, P.; Best, A. S. Conducting-Polymer-Based Supercapacitor Devices and Electrodes. *J. Power Sources* **2011**, *196*, 1–12.

114. Druschler, M.; Borisenko, N.; Wallauer, J.; Winter, C.; Huber, B.; Endres, F.; Roling, B. New Insights into the Interface between a Single-Crystalline Metal Electrode and an Extremely Pure Ionic Liquid: Slow Interfacial Processes and the Influence of Temperature on Interfacial Dynamics. *Phys. Chem. Chem. Phys.* **2012**, *14*, 5090–5099.
115. Cannes, C.; Cachet, H.; Debiemme-Chouvy, C.; Deslouis, C.; de Sanoit, J.; Le Naour, C.; Zinovyeva, V. A. Double Layer at [Bumeim][Tf2N] Ionic Liquid−Pt or −C Material Interfaces. *J. Phys. Chem. C* **2013**, *117*, 22915–22925.
116. Hu, Z.; Vatamanu, J.; Borodin, O.; Bedrov, D. A Molecular Dynamics Simulation Study of the Electric Double Layer and Capacitance of [Bmim][PF6] and [Bmim][BF4] Room Temperature Ionic Liquids near Charged Surfaces. *Phys. Chem. Chem. Phys.* **2013**, *15*, 14234–47.
117. Vatamanu, J.; Xing, L.; Li, W.; Bedrov, D. Influence of Temperature on the Capacitance of Ionic Liquid Electrolytes on Charged Surfaces. *Phys. Chem. Chem. Phys.* **2014**, *16*, 5174–82.
118. Vatamanu, J.; Borodin, O.; Smith, G. D. Molecular Insights into the Potential and Temperature Dependences of the Differential Capacitance of a Room-Temperature Ionic Liquid at Graphite Electrodes. *J. Am. Chem. Soc.* **2010**, *132*, 14825–33.
119. Peres, C. High Power Electric Double-Layer Capacitors Based on Room-Temperature Ionic Liquids and Nanostructured Carbons, Ph.D. Thesis. Drexel University: Philadelphia, PA, 2013; http://hdl.handle.net/1860/4209. See Figure 13, page 25.
120. Zetterström, P.; Urbonaite, S.; Lindberg, F.; Delaplane, R. G.; Leis, J.; Svensson, G. Reverse Monte Carlo Studies of Nanoporous Carbon from Tic. *J. Phys.: Condens. Matter* **2005**, *17*, 3509–3524.
121. Jain, S. K.; Pellenq, R. J. M.; Pikunic, J. P.; Gubbins, K. E. Molecular Modeling of Porous Carbons Using the Hybrid Reverse Monte Carlo Method. *Langmuir* **2006**, *22*, 9942–9948.
122. Pikunic, J.; Clinard, C.; Cohaut, N.; Gubbins, K. E.; Guet, J.-M.; Pellenq, R. J. M.; Rannou, I.; Rouzaud, J.-N. Structural Modeling of Porous Carbons: Constrained Reverse Monte Carlo Method. *Langmuir* **2003**, *19*, 8565–8582.
123. Vatamanu, J.; Borodin, O.; Bedrov, D.; Smith, G. D. Molecular Dynamics Simulation Study of the Interfacial Structure and Differential Capacitance of Alkylimidazolium Bis(Trifluoromethanesulfonyl)Imide [Cnmim][TFSI] Ionic Liquids at Graphite Electrodes. *J. Phys. Chem. C* **2012**, *116*, 7940–7951.
124. Vatamanu, J.; Borodin, O.; Smith, G. D. Molecular Simulations of the Electric Double Layer Structure, Differential Capacitance, and Charging Kinetics for *N*-Methyl-*N*-Propylpyrrolidinium Bis(Fluorosulfonyl)Imide at Graphite Electrodes. *J. Phys. Chem. B* **2011**, *115*, 3073–3084.
125. Reed, S. K.; Lanning, O. J.; Madden, P. A. Electrochemical Interface between an Ionic Liquid and a Model Metallic Electrode. *J. Chem. Phys.* **2007**, *126*, 084704.
126. Vatamanu, J.; Borodin, O.; Smith, G. D. Molecular Dynamics Simulations of Atomically Flat and Nanoporous Electrodes with a Molten Salt Electrolyte. *Phys. Chem. Chem. Phys.* **2010**, *12*, 170–182.
127. Reed, S. K.; Madden, P. A.; Papadopoulos, A. Electrochemical Charge Transfer at a Metallic Electrode: A Simulation Study. *J. Chem. Phys.* **2008**, *128*, 124701.
128. Siepmann, J. I.; Sprik, M. Influence of Surface Topology and Electrostatic Potential on Water/Electrode Systems. *J. Chem. Phys.* **1995**, *102*, 511–524.
129. Golze, D.; Iannuzzi, M.; Nguyen, M.-T.; Passerone, D.; Hutter, J. Simulation of Adsorption Processes at Metallic Interfaces: An Image Charge Augmented Qm/Mm Approach. *J. Chem. Theory Comput.* **2013**, *9*, 5086–5097.
130. Kawata, M.; Mikami, M. Rapid Calculation of Two-Dimensional Ewald Summation. *Chem. Phys. Lett.* **2001**, *340*, 157–164.
131. Kawata, M.; Mikami, M.; Nagashima, U. Computationally Efficient Method to Calculate the Coulomb Interactions in Three-Dimensional Systems with Two-Dimensional Periodicity. *J. Chem. Phys.* **2002**, *116*, 3430–3448.
132. Kawata, M.; Mikami, M.; Nagashima, U. Rapid Calculation of the Coulomb Component of the Stress Tensor for Three-Dimensional Systems with Two-Dimensional Periodicity. *J. Chem. Phys.* **2001**, *115*, 4457–4462.
133. Kawata, M.; Nagashima, U. Particle Mesh Ewald Method for Three-Dimensional Systems with Two-Dimensional Periodicity. *Chem. Phys. Lett.* **2001**, *340*, 165–172.
134. Vatamanu, J.; Borodin, O.; Smith, G. D. Molecular Dynamics Simulation Studies of the Structure of a Mixed Carbonate/LiPF6 Electrolyte near Graphite Surface as a Function of Electrode Potential. *J. Phys. Chem. C* **2011**, *116*, 1114–1121.
135. Xing, L.; Vatamanu, J.; Borodin, O.; Smith, G. D.; Bedrov, D. Electrode/Electrolyte Interface in Sulfolane-Based Electrolytes for Li Ion Batteries: A Molecular Dynamics Simulation Study. *J. Phys. Chem. C* **2012**, *116*, 23871–23881.
136. Pastewka, L.; Järvi, T. T.; Mayrhofer, L.; Moseler, M. Charge-Transfer Model for Carbonaceous Electrodes in Polar Environments. *Phys. Rev. B: Condens. Matter Mater. Phys.* **2011**, *83*, 165418.
137. Wang, Z.; Yang, Y.; Olmsted, D. L.; Asta, M.; Laird, B. B. Evaluation of the Constant Potential Method in Simulating Electric Double-Layer Capacitors. *J. Chem. Phys.* **2014**, *141*, 184102.
138. Kiss, P. T.; Sega, M.; Baranyai, A. Efficient Handling of Gaussian Charge Distributions: An Application to Polarizable Molecular Models. *J. Chem. Theory Comput.* **2014**, *10*, 5513–5519.
139. Martyna, G. J.; Tuckerman, M. E.; Tobias, D. J.; Klein, M. L. Explicit Reversible Integrators for Extended Systems Dynamics. *Mol. Phys.* **1996**, *87*, 1117–1157.
140. Hoover, W. G. Canonical Dynamics: Equilibrium Phase-Space Distributions. *Phys. Rev. A: At., Mol., Opt. Phys.* **1985**, *31*, 1695–1697.
141. Vatamanu, J.; Kusalik, P. G. Molecular Dynamics Methodology to Investigate Steady-State Heterogeneous Crystal Growth. *J. Chem. Phys.* **2007**, *126*, 124703.